Disruption of Synaptic Endoplasmic Reticulum Luminal Protein Containment in *Drosophila Atlastin* Mutants

Mónica C. Quiñones-Frías[1], Dina M. Ocken[1] and Avital Rodal[1,*]

[1]Department of Biology, Brandeis University, Waltham, MA

*Corresponding author:

Email: arodal@brandeis.edu

Abstract:

The endoplasmic reticulum (ER) extends throughout neurons and regulates many neuronal functions, including neurite outgrowth, neurotransmission, and synaptic plasticity. Mutations in proteins that control ER shape are linked to the neurodegenerative disorder Hereditary Spastic Paraplegia (HSP), yet the ultrastructure and dynamics of neuronal ER remain largely unexplored, especially at presynaptic terminals. Using super-resolution and live imaging in *D. melanogaster* larval motor neurons, we investigated ER structure at presynaptic terminals of wild-type animals and null mutants of the ER shaping protein and HSP-linked gene, Atlastin. Previous studies using an ER luminal marker reported diffuse localization at *Atlastin* mutant presynaptic terminals, which was attributed to ER fragmentation. However, using an ER membrane marker, we discovered that *Atlastin* mutant ER forms robust networks with only mild defects in structural dynamics, indicating the primary defect is functional rather than architectural. We demonstrate that *Atlastin* mutants progressively displace overexpressed luminal ER proteins to the cytosol during larval development, specifically at synapses, while these proteins remain correctly localized in cell bodies, axons, and muscles. This synaptic-specific displacement phenotype, previously unreported in non-neuronal cells, emphasizes the importance of studying neurons to understand HSP pathogenesis.

Introduction:

The endoplasmic reticulum (ER) is a continuous organelle that extends to the periphery of neurons and regulates many neuronal functions, including neurite outgrowth, neurotransmission, and synaptic plasticity (de Juan-Sanz et al., 2017; Liu et al., 2019; Oliva et al., 2020; Perez-Alvarez et al., 2020; Raffaello et al., 2016; Raiborg et al., 2015). Structurally, this essential organelle consists of two domains: ER sheets (enriched in cell bodies) and ER tubules (abundant in dendrites and axons) (Öztürk et al., 2020; Wu et al., 2017). Recent studies

have revealed even finer levels of organization, with increasing evidence to suggest further structural and functional differences in neuronal ER tubules. For instance, different regions of the neuron show distinct features, including varying densities of ER-organelle contacts (Wu et al., 2017), specialized ER-endosome contacts that regulate lysosome size in cell bodies (Özkan et al., 2021), and unique ER ladder structures in developing axons and dendrites (Benedetti et al., 2024; Zamponi et al., 2022). These regional specializations underscore the importance of examining ER structure and function across all neuronal regions. However, the cell biology and ultrastructure of the neuronal ER, particularly at presynaptic terminals, have been under-investigated. Conventional microscopy, used in most studies of neuronal ER structure, lacks the resolution needed to visualize individual ER tubules in small structures like presynaptic terminals (Chouhan et al., 2010; Oliva et al., 2020; Orso et al., 2009; Pérez-Moreno et al., 2023; Summerville et al., 2016; Yalçın et al., 2017). Other techniques such as electron microscopy (EM) have typically been limited to thin 2D sampling and cannot be used in live samples. These limitations make it difficult to distinguish the ER from synaptic vesicles at synapses and prevent the examination of live dynamics (Orso et al., 2009; Wu et al., 2017; Zhu et al., 2022).

We must overcome the technical challenges of studying neuronal ER as mutations in ER-shaping genes cause neurodegenerative disorders such as Hereditary Spastic Paraplegia (HSP) and Charcot Marie Tooth Disease, indicating that ER structure is uniquely essential for neuronal physiology (Boutry et al., 2019; Fowler et al., 2019; Öztürk et al., 2020). One essential ER tubule-shaping protein is Atlastin, a GTPase that regulates the homotypic fusion and tethering of ER tubules to form 3-way junctions (Lü et al., 2020). In humans, mutations in *Atlastin* underlie one of the most common forms of autosomal dominant HSP, highlighting the importance of examining its neuron-specific functions in regulating ER structure (Finsterer et al., 2012). In various experimental systems, *Atlastin* mutants exhibit numerous neuronal phenotypes, including defects in synaptic vesicle cycling and trafficking of neuronal cargoes (Gregorio et al., 2017), synapse development (Gregorio et al., 2017; Lee et al., 2009; Zhu et al., 2006), and axon regeneration (Rao et al., 2016). However, significant gaps remain in our understanding of how Atlastin-dependent changes in the structure and dynamics of neuronal ER lead to these functional defects. For example, using electron microscopy others found *Drosophila Atlastin* mutants exhibited shorter ER tubules in their motor neuron cell bodies(Orso et al., 2009) and diffuse localization of an ER lumen marker in their presynaptic terminals, attributed to extensive ER fragmentation (Summerville et al., 2016). However, this fragmentation has not been validated

by EM or by fluorescence using ER membrane markers. Further, in *C. elegans, Atlastin* mutant ER networks in neuronal dendrites were not fragmented but were prone to retraction, leading to disrupted microtubule structures and mitochondrial fission (Liu et al., 2019). Finally, a ladder-like ER expansion was observed in spinal axons in a mouse model of Atlastin-dependent HSP (Zhu et al., 2022). In contrast to these neuronal findings, knockdown of Atlastin in Hela or Cos-7 cells leads to long and unbranched ER tubules (Hu et al., 2009, 2015; Niu et al., 2019). Thus, loss of Atlastin causes distinct ER phenotypes depending on several factors, including cell type, which region of the neuron was examined, and the reporter used to visualize the ER. To resolve the functions of this vital protein, comprehensive imaging studies of ER organization in the different regions of the neuron are needed, using complementary labeling strategies.

Another critical gap is our limited understanding of neuronal ER dynamics. High-resolution imaging in non-neuronal cells has revealed transitions from ER tubules to ER sheets (Lu et al., 2009; Sun et al., 2011), ER fragmentation (Espadas et al., 2019), tubule extension and retraction (Friedman et al., 2011; Hoyer et al., 2018; Rowland et al., 2014), and alterations in the number of 3-way junctions (Spits and Neefjes, 2021). These dynamics have been linked to ER functions such as endosome or mitochondrial fission (Friedman et al., 2011; Hoyer et al., 2018; Rowland et al., 2014) and calcium signaling (Crapart et al., 2023; Sun et al., 2011). In neurons, ER rearrangements have been suggested to alter calcium compartmentalization (Subramanian and Meyer, 1997), local protein synthesis (Deng et al., 2021; Schwarz and Blower, 2016), organelle contacts (Lu et al., 2020) and transport within the ER (Scott et al., 2021). However, the types and functions of neuronal ER dynamics, particularly in presynaptic terminals, remain largely unknown due to the challenges of imaging ER networks over time in small compartments. New insights into the mechanisms that regulate ER structure and ER dynamics in neurons are crucial for understanding why and how mutations in ER shaping proteins, such as Atlastin, predominantly affect the nervous system. Here, we addressed this gap by examining the structure and dynamics of the ER at the *Drosophila* neuromuscular junction (NMJ) of wild-type and *Atlastin* mutants using *in vivo* imaging and super-resolution Airyscan microscopy.

98 **Results**

99

100 High resolution imaging of the ER in *Drosophila* motor neuron cell bodies, axons, and
101 presynaptic terminals.

102

103 At presynaptic terminals of the *Drosophila* larval NMJ, the ER is highly sensitive to
104 fixation, limiting imaging experiments to live samples, often acquired on upright microscopes
105 using water dipping objectives (Chouhan et al., 2010; Oliva et al., 2020; O'Sullivan et al., 2012;
106 Pérez-Moreno et al., 2023; Summerville et al., 2016; Yalçın et al., 2017). However, the axial
107 resolution limit of typical water dipping objectives is >300 nm, which cannot distinguish the
108 densely packed ER tubules at presynaptic terminals (Espadas et al., 2019; Wu et al., 2017). To
109 overcome this limitation, we created a reusable microscopy imaging slide to capture live super-
110 resolution images or movies of neuronal ER in *Drosophila* larval fillets through glass coverslips,
111 utilizing high numerical aperture oil objectives and Airyscan microscopy (**Figure 1A**). Our system
112 provides an axial resolution of ~170 nm after image processing (Del Signore et al., 2022). We
113 imaged larval fillets using this imaging slide on both inverted and upright microscopes within 40-
114 50 min from dissection, a time frame in which this preparation maintains muscle potential and
115 the capacity for evoked neurotransmitter release, even once the axon is severed from the cell
116 body (Feng et al., 2004).

117

118 To study the live dynamics of the ER, we used Vglut-Gal4 to express either the luminal
119 ER marker BiP:sfGFP:HDEL (**Figure 1B-D**, **2C**) or the transmembrane ER marker
120 tdTomato:Sec61β (**Figure 2B**) in *Drosophila* 3rd instar larval motor neurons. These markers were
121 previously shown to co-localize at this synapse, indicating they are comparable reporters for
122 visualizing synaptic ER (Summerville et al., 2016). Our imaging approach allowed more precise
123 visualization of ER tubules and networks labeled by these reporters in cell bodies, axons, and
124 presynaptic terminals compared to previously reported results (**Figure 1B-D, 2**). As previously
125 observed using lower-resolution imaging (Summerville et al., 2016), we detected ER tubule
126 structures in all neuronal regions examined, including ER tubules and ER sheets in cell bodies,
127 and ER tubules in axons and presynaptic terminals. In axons, ER tubules were long, and we
128 sometimes observed a ladder-like structure consisting of pairs of interconnected ER tubules
129 joined by rungs or cross-bridges, similar to structures previously described in developing axons
130 of mammalian cultured neurons and *Drosophila* dendrites (Benedetti et al., 2024; Zamponi et

al., 2022) (**Figure 1C**). At presynaptic terminals, ER tubules in some boutons appeared in a highly interconnected basket-like network, while others were transversed by several parallel ER tubules, similar to the ladder-like structures observed in axons (**Figure 1D**). Using this improved imaging approach, we achieved high-resolution visualization of individual ER tubules within networks of *Drosophila* presynaptic terminals, enabling detailed analysis of their structure and dynamics over time.

We next examined ER dynamics in *en passant* and terminal boutons at the *Drosophila* NMJ (**Figure 2A**). Terminal boutons have distinct cytoskeletal organization and signaling that could regulate the dynamics of the ER differently (Deshpande et al., 2016; Fernandes et al., 2023; Roos et al., 2000). To examine the dynamics of the ER at presynaptic terminals, we collected Z stacks of single boutons expressing the ER membrane marker for 40 sec at 0.92 sec/stack (**Movie S1-S3**) or the luminal ER marker for 90 sec at 0.73 sec/stack (**Movie S4-S6**). Both markers were distributed unevenly across the ER network (**Figure 2B-2C**). In particular, the luminal ER marker exhibited numerous discrete round foci that moved within ER tubules with fast dynamics (<1 sec) (**Figure 2C**). These foci were less frequently observed with the ER membrane marker (**Figure 2B**, **bottom**), consistent with the model that proteins in the ER lumen and ER membrane may differentially cluster and move within the ER (Holcman et al., 2018; Obara et al., 2024). Conversely, static regions of high intensity (which we saw for both markers) may reflect stacked ER tubules (Costantini et al., 2012).

We focused on the ER membrane marker to define dynamic events since its labeling pattern had fewer confounding foci. Analysis revealed three distinct types of ER dynamics: (1) ER budding events, in which a fragment of ER dissociates from the network; (2) Focus dynamics, in which round foci move within the ER network; and (3) ER tubule dynamics, including overall displacement of the tubule in the XY plane, as well as lengthening (extension) and shortening (retraction) of the tubule (**Figure 2D**). We qualitatively categorized boutons as “static” if we observed no change in ER network structure or “dynamic” if we observed at least one change. On many occasions, we observed multiple types of ER dynamics within the same bouton. We found that terminal boutons are highly dynamic (89%) while *en passant* boutons were moderately dynamic (38%) (**Figure 2E**). This difference in dynamics suggests that the ER is regulated differently in different regions of presynaptic terminals and could have specialized functions.

164

165 Next, we characterized the frequency of the three main types of ER network dynamics at
166 terminal boutons, where we observed the most remodeling. Among terminal boutons, 93%
167 exhibited tubule movements, making this the most common type of ER remodeling (**Figure 2F**).
168 Less frequently, we observed that 28% of boutons had ER budding and 12% had moving foci.
169 We further classified tubule movements into four categories: displacement, extension, retraction,
170 and extension followed by retraction. The most common category was extension followed by
171 retraction, observed in 81% of terminal boutons (**Figure 2G**). Simple displacement occurred in
172 44% of boutons, 24% showed extension alone, and 18% showed retraction alone. These results
173 demonstrate our ability to capture diverse ER behaviors at high resolution in live *Drosophila*
174 motor neurons.

175

176 <u>Presynaptic terminals of *Atlastin* mutants form robust ER networks.</u>

177 To investigate the relationship between ER structure and function at synapses, we
178 examined mutants of Atlastin, a GTPase that regulates ER tubule fusion. *Drosophila* has a single
179 homolog while mammals have three Atlastin homologs, with Atlastin-1 enriched in the brain
180 (Rismanchi et al., 2008). The diverse neuronal phenotypes in *Atlastin* mutants, including defects
181 in synaptic growth, vesicle cycling, cargo trafficking, and axon regeneration, make it an excellent
182 model for understanding how ER architecture impacts cellular function (Audhya et al., 2007;
183 Gregorio et al., 2017; Lee et al., 2009; Rao et al., 2016; Zhu et al., 2006). We analyzed
184 transheterozygotes of an *Atlastin* null allele (atl^2) and a deficiency removing the *Atlastin* locus to
185 avoid second-site effects (Lee et al., 2009). These *Atlastin* null mutants (hereafter referred to as
186 *Atlastin* mutants) were mainly pharate lethal and showed increased satellite boutons at larval
187 NMJs (**Figure 3A-B**), indicating defects in synaptic development as previously reported
188 (Gregorio et al., 2017; Lee et al., 2009).

189

190 Using confocal microscopy, Summerville et al. (2016) observed that the ER lumen marker
191 BiP:sfGFP:HDEL was diffusely distributed in *Atlastin* mutant presynaptic terminals and
192 concluded that the ER was extensively fragmented. To ask whether an ER membrane marker
193 would show similar fragmentation, we used spinning disk and Airyscan microscopy to examine
194 ER network structures at *Atlastin* mutant presynaptic terminals expressing the ER membrane
195 marker tdTomato:Sec61β. We found that tdTomato:Sec61β labeled intact ER networks in
196 *Atlastin* mutant synapses (**Figure 3A**, **Figure 3_Supplement**). Our results suggest that ER

197 networks exist in *Atlastin* mutant presynaptic terminals, and the previously observed defects in
198 synaptic function are likely due to more subtle ER structural or dynamic properties rather than
199 fragmentation. However, we found that the marker tdTomato:Sec61β exhibited lower
200 fluorescence levels in *Atlastin* mutants, as quantified by its mean intensity within the entire
201 presynaptic terminal in fixed preparations (**Figure 3C**). This reduction in ER membrane marker
202 intensity has also been observed in other HSP mutants, suggesting this is a common feature of
203 ER shaping mutants and could indicate changes in ER membrane composition, integrity, or
204 tubule thickness (Pérez-Moreno et al., 2023). We also noted that the coefficient of variation
205 (CoV) of tdTomato:Sec61β signal was significantly higher in *Atlastin* mutants (**Figure 3D**),
206 suggesting that it is more concentrated in subsynaptic structures compared to wild-type
207 synapses (notably the opposite of what would be expected for fragmentation).
208
209 Next, we measured the levels of tdTomato:Sec61β in various motor neuron regions to
210 determine if its reduced levels are specific to presynaptic terminals or a cell-wide phenotype
211 (**Figure 4**). Using Vglut-Gal4 to label motor neurons, we measured clusters of cell bodies in the
212 ventral ganglion and axon bundles extending towards body-wall muscles (**Figure 4A-B**). *Atlastin*
213 mutants have significantly increased tdTomato:Sec61β intensity levels in axon bundles (**Figure**
214 **4C**) and unchanged levels in cell body clusters (**Figure 4F**). We also found that the volume
215 occupied by tdTomato:Sec61β-labeled structures was significantly increased in axon bundles
216 and decreased in cell body clusters of *Atlastin* mutants. Finally, we observed a significant
217 decrease in the CoV of the tdTomato:Sec61β signal in both axon bundles and cell body clusters,
218 suggesting less concentrated ER structures (the opposite of what we observed at presynaptic
219 terminals). Our results suggest that the changes observed in cell body clusters, axon bundles,
220 and presynaptic terminals are local, indicating that the ER has neuronal region-specific
221 phenotypes regulated by Atlastin. These changes in tdTomato:Sec61β distribution could reflect
222 alterations in ER structure or ER membrane protein density.
223
224 <u>*Atlastin* mutants show mild defects in synaptic ER dynamics</u>
225 We hypothesized that Atlastin could regulate synaptic function by controlling the
226 dynamics of the ER network. We captured rapid time-lapse images of the ER labeled with
227 tdTomato:Sec61β in *en passant* and terminal boutons at 0.92 sec/stack (**Figure 2D-G, Figure**
228 **5A**, **Movies 7-14**). We blinded movies from controls and *Atlastin* mutants to qualitatively

229 categorize boutons as “dynamic” or “static”, as described above (**Figure 2E**). Compared to the
230 89% of terminal boutons in control animals that exhibited dynamics (previously shown in **Figure**
231 **2B, E**), we found a small but significant reduction in dynamic boutons in *Atlastin* mutants (76%),
232 with a concomitant increase in the fraction of non-dynamic boutons (24%) (**Figure 5B**). In *en*
233 *passant* boutons, we observed similar ER dynamics in controls (62% static/38% dynamic) and
234 *Atlastin* mutants (69% static/31% dynamic). These findings indicate that *Atlastin* mutants exhibit
235 mild defects in ER dynamics, specifically at terminal boutons, with no significant changes in *en*
236 *passant* boutons. This suggests that Atlastin's ER tubule tethering and fusion roles are critical in
237 highly dynamic ER networks like those found in terminal boutons.
238
239 We performed a further comprehensive analysis of ER dynamics in *Atlastin* mutants,
240 examining multiple structural rearrangements, including tubule dynamics, ER budding, and the
241 movement of concentrated protein foci. Surprisingly, despite Atlastin being the sole homolog in
242 *Drosophila* and a key player in ER membrane fusion, we found only modest changes in ER
243 structure and dynamics. While we observed slight shifts in the relative frequencies of different
244 dynamic events (**Figure 5C-D, Figure 5A-Supplement**), none of these changes reached
245 statistical significance, and the overall dynamic capacity of the ER network remained intact
246 (**Figure 5B-Supplement**). The subtlety of these phenotypes suggests either substantial
247 functional redundancy with other ER-shaping proteins or the existence of compensatory
248 mechanisms that maintain ER organization and dynamics in neurons upon loss of *Atlastin*.
249 Moreover, given the numerous synaptic defects previously reported in *Atlastin* mutants, our
250 findings suggest that these phenotypes may arise from defects in ER function rather than gross
251 changes in ER structure or dynamics.
252
253 <u>*Atlastin* mutant presynaptic terminals exhibit distinct BiP:sfGFP:HDEL and tdTomato:Sec61β</u>
254 <u>distributions.</u>
255
256 Our results showing intact ER networks in *Atlastin* mutants using an ER membrane
257 marker sharply contrast with those from a prior study examining *Atlastin* mutants using the
258 luminal marker BiP:sfGFP:HDEL, where its diffuse distribution was interpreted as ER
259 fragmentation (Summerville et al., 2016). To further explore this discrepancy, we used Airyscan
260 microscopy to re-examine BiP:sfGFP:HDEL in *Atlastin* mutants. Unlike its strict localization to
261 the ER network in control synapses, we reproduced the observation that a significant fraction of

262 BiP:sfGFP:HDEL was diffusely localized in *Atlastin* mutant synapses, even at the resolution of
263 Airyscan microscopy. Further, the marker filled the interiors of boutons and extended to their
264 periphery, suggesting that it may be mislocalized to the cytosol instead of within ER fragments
265 (**Figure 6A-B**).
266
267 We identified two distinct ER network phenotypes in *Atlastin* mutants: NMJs with "Partial
268 loss" had both diffuse BiP:sfGFP:HDEL and an identifiable ER network structure, while NMJs
269 with "Complete loss" had a more severe phenotype with no visible ER network structures. We
270 blinded our images and categorized control and *Atlastin* mutant datasets as "Partial loss,"
271 "Complete loss," or "No phenotype" (**Figure 6C**). In *Atlastin* mutants, we found that 45% of NMJs
272 exhibited partial loss, 55% exhibited complete loss, and 10% had no phenotype. We observed
273 partial loss and complete loss phenotypes in both anterior (segment A2) and posterior (segment
274 A5) muscle segments, in Is (phasic) and Ib (tonic) motor neuron subtypes, and in neurons
275 innervating multiple different body wall muscles, suggesting that it reflects a widespread
276 phenomenon in NMJs of *Atlastin* mutants (**Figure 6 - Figure 6-Supplement**). Presynaptic
277 terminals in *Atlastin* mutants show similar mean intensities of the luminal ER marker compared
278 to controls, suggesting that the marker's redistribution in mutant neurons does not affect its
279 overall levels (**Figure 6D-E**). However, we observed a significant change in the CoV in *Atlastin*
280 mutants due to the redistribution of the luminal marker (**Figure 6F**). Along with our earlier finding
281 that the ER membrane marker, tdTomato:Sec61β, does not exhibit fragmentation, these results
282 suggest the possibility that the luminal ER marker is displaced to the cytosol.
283
284 *Atlastin* mutants may be particularly sensitized to overexpression of the BiP:sfGFP:HDEL
285 marker because we could not assess the co-localization of BiP:sfGFP:HDEL and
286 tdTomato:Sec61β, as very few larvae co-expressing these markers survived. The few that did
287 had grossly defective NMJ morphologies and large aggregates of both markers, even in wild-
288 type flies (data not shown). Further, control adult flies expressing BiP:sfGFP:HDEL were
289 unhealthy and could not be maintained as a stock, suggesting that this marker is toxic.
290
291 Next, we asked whether the luminal ER marker displacement phenotype is specific to all
292 neuronal regions or specific to presynaptic terminals. First, we examined the ER in body wall
293 muscles of *Atlastin* mutants by overexpressing the BiP:sfGFP:HDEL with the muscle driver
294 BG57-Gal4. We did not find the luminal ER marker displaced to the cytosol (**Figure 7, right**).

295 However, as noted in earlier studies (Lee et al., 2009), we observed a decrease in network
296 complexity. Next, we examined the cell body and axons of *Atlastin* mutants to determine if the
297 displacement of the luminal ER marker was a global or local phenotype within neurons. As
298 previously reported (Summerville et al., 2016), we did not observe a diffuse signal for the luminal
299 ER marker in cell bodies or distal axons (within ~30µm of the synapse) (**Fig 7, middle + left**).
300 However, we did observe ER fragmentation in some axons (**Fig 7, left**). These results indicate
301 that the displacement of BiP:sfGFP:HDEL in *Atlastin* mutants is a synapse-specific phenotype.
302
303 The luminal ER phenotype in *Atlastin* mutants is progressive
304
305 Atlastin dysfunction is linked to the neurodegenerative disorder HSP, in which patients
306 progressively lose neuronal function over time (Blackstone, 2018, 2012; Blackstone et al., 2011).
307 *Drosophila Atlastin* mutants recapitulate progressive motor dysfunction as observed in HSP
308 patients (Gregorio et al., 2017). We examined 1st instar larvae to test the hypothesis that the
309 partial loss phenotype may similarly progress to the complete loss phenotype through larval
310 development. We categorized control and *Atlastin* mutant datasets as described above (**Figure**
311 **6**). We anticipated that a progressive phenotype would decrease the proportion of NMJs showing
312 BiP:sfGFP:HDEL displacement and an increase in presynaptic terminals displaying no
313 phenotype. Indeed, we observed that the percentage of NMJs with complete loss increased from
314 12.5% in 1st instar to 55% in 3rd instar, while NMJs with no phenotype decreased from 38% to
315 10% across these developmental stages (compare **Figure 8A-C** to **Figure 6**). These results
316 suggest that displacement of the luminal ER marker progresses over time and that this
317 phenotype is initiated early in neuronal development.
318
319 *Atlastin* mutants have disrupted luminal ER protein dynamics
320
321 To examine ER network continuity and the dynamic properties of luminal ER proteins in
322 *Atlastin* mutants, we used fluorescence recovery after photobleaching (FRAP) to track
323 BiP:sfGFP:HDEL mobility at presynaptic terminals (**Figure 9A**). In this analysis, the rate and
324 extent of fluorescence recovery provide key insights into protein behavior: continuous ER
325 networks show robust recovery due to the movement of unbleached proteins across the
326 connected network, while fragmented ER networks fail to recover due to physical barriers
327 between compartments (Dayel et al., 1999; Lippincott-Schwartz et al., 2018). Further, if the

328 BiP:sfGFP:HDEL protein had leaked into the cytosol, we would expect rapid recovery due to the
329 higher diffusion rates of cytosolic proteins compared to ER-localized proteins (Dayel et al.,
330 1999). Our FRAP analysis examined single synaptic boutons co-expressing BiP:sfGFP:HDEL
331 and RFP:mCD8, which labels the neuronal plasma membrane. We photobleached *en passant*
332 boutons in the middle of a synaptic branch to ensure BiP:sfGFP:HDEL could recover from ER
333 networks surrounding the FRAP region. We recorded movies of a single NMJ slice,
334 simultaneously imaging both markers. After photobleaching with a 405nm laser, we captured
335 recovery dynamics by imaging every 10 seconds for 2 minutes (**Figure 9, Movies 15-19**).
336
337 We analyzed the recovery after photobleaching of RFP:mCD8 and BiP:sfGFP:HDEL to
338 characterize protein dynamics in *Atlastin* mutant presynaptic terminals. RFP:mCD8 served as a
339 control because it showed similar plasma membrane distribution patterns at synaptic boutons in
340 both control and *Atlastin* mutants, suggesting that plasma membrane organization was
341 unaffected and would exhibit comparable dynamics across all genotypes. While the recovery of
342 RFP:mCD8 could not be fitted to a non-linear equation due to the absence of a plateau, its similar
343 recovery across genotypes indicates no significant changes in its diffusion at the plasma
344 membrane (**Figure 9B-C**). We next analyzed BiP:sfGFP:HDEL recovery using a one-association
345 non-linear model, focusing first on the plateau to estimate the mobile fraction of the luminal ER
346 marker in the FRAP region (**Figure 9B, D**). We found that *Atlastin* mutants with partial loss of
347 ER networks had the least recovery, with a mobile fraction of 50.61%. By contrast, controls and
348 *Atlastin* mutants with complete loss had a higher mobile fraction of 65.73% and 66.34%,
349 respectively. We also measured how quickly BiP:sfGFP:HDEL recovered by calculating the time
350 to reach 50% of maximum recovery. *Atlastin* mutants with partial loss exhibited the slowest
351 BiP:sfGFP:HDEL recovery, reflected by a longer half-life (38.26 sec) compared to controls
352 (26.91 sec), while those with complete loss had the fastest recovery (14.62 sec). The reduced
353 mobile fraction in partial loss *Atlastin* mutants likely reflects discontinuous ER networks (**Figure**
354 **9B**, blue arrows). In contrast, the rapid recovery and absence of visible ER structures in complete
355 loss *Atlastin* mutants suggests that BiP:sfGFP:HDEL is largely displaced into the cytosol. Our
356 analyses indicate that Atlastin dysfunction impairs luminal ER protein diffusion and subcellular
357 localization. Surprisingly, these defects occur while maintaining relatively normal synaptic ER
358 network structure (**Figure 3-4**) and dynamics (**Figure 5**). These findings reveal a novel
359 pathogenic mechanism where Atlastin dysfunction primarily impacts ER protein distribution

360 rather than ER network morphology, potentially disrupting synaptic function through the
361 mislocalization of essential ER proteins.
362
363 Luminal proteins are displaced to the cytosol at presynaptic terminals of *Atlastin* mutants
364
365 A fundamental question emerged from our observations: does the altered
366 BiP:sfGFP:HDEL distribution in *Atlastin* mutants arise from ER fragmentation or genuine protein
367 displacement to the cytosol? Previous research shows that ER network morphology relies on a
368 delicate balance between ER shaping proteins; disrupting this balance may result in ER
369 fragmentation (Wang et al., 2016). In contrast, the displacement of luminal proteins to the cytosol
370 suggests changes in the ER integrity and potential activation of ER stress responses (Merighi
371 and Lossi, 2022). To definitively distinguish between these models, we conducted two
372 independent experiments to track BiP:sfGFP:HDEL sub-cellular localization at presynaptic
373 terminals. First, we examined whether BiP:sfGFP:HDEL in *Atlastin* mutants is sensitive to the
374 mild detergent digitonin, which gently permeabilizes the plasma membrane and extracts proteins
375 from the cytosol but not the ER (Le Gall et al., 2004). Second, we examined the direct interaction
376 between BiP:sfGFP:HDEL and a plasma membrane-tethered nanobody, which would only occur
377 if the protein was displaced to the cytosol.
378
379 We hypothesized that digitonin treatment would lead to loss of fluorescence in *Atlastin*
380 mutants, proportional to the fraction of the luminal ER marker protein in the cytosol (**Figure 10B-**
381 **Supplement**). We treated presynaptic terminals for 5 min with digitonin (**Figure 10A-**
382 **Supplement**) and imaged the same presynaptic terminal (expressing either cytosolic GFP or
383 BiP:sfGFP:HDEL) before and after digitonin treatment. We also labeled our live samples with α-
384 HRP antibodies to identify presynaptic terminals (Snow et al., 1987). We measured the fraction
385 change in mean intensity to determine the effects of digitonin treatment on cytosolic and ER
386 markers (**Figure 10C-Supplement**). We observed a significant loss in mean fluorescence of
387 cytosolic GFP following digitonin treatment. Control presynaptic terminals expressing the luminal
388 ER marker BiP:sfGFP:HDEL became highly fragmented, possibly due to osmolarity changes in
389 the cytosol, which are known to promote ER fragmentation (King et al., 2020). Despite this
390 fragmentation, most ER remained within the synaptic terminal, suggesting limited extraction or
391 permeabilization by this treatment. In half the control samples, the marker redistributed to bright
392 puncta and showed an unexpected increase in mean intensity. One interpretation is that digitonin

393 treatment allows the exchange of small molecules into the ER (Le Gall et al., 2004), potentially
394 altering the fluorescent properties of sfGFP. The other half of the samples had slightly reduced
395 mean intensity following digitonin treatment, possibly due to moderate loss of ER fragments. We
396 next analyzed *Atlastin* mutants categorized as "Partial loss" or "Complete loss". Digitonin
397 treatment yielded no significant differences between controls and *Atlastin* mutants with partial
398 loss. We also observed that *Atlastin* mutant synapses exhibiting partial loss had puncta following
399 digitonin treatment that were similar to the control. This is likely because the partial loss
400 presynaptic terminals have some ER network visible with the luminal marker. In contrast, we
401 observe a significant decrease in fluorescence intensity following digitonin treatment in *Atlastin*
402 mutant presynaptic terminals with complete loss, which do not exhibit visible ER networks, as
403 indicated by the luminal marker. These results suggest that luminal ER molecules in *Atlastin*
404 mutants are likely displaced to the cytosol.
405
406 From the digitonin experiments, we cannot rule out the possibility that BiP:sfGFP:HDEL
407 resides in small ER membrane fragments that easily diffuse out of permeabilized plasma
408 membranes. We hypothesized that if BiP:sfGFP:HDEL is displaced to the cytosol in *Atlastin*
409 mutants, it would interact with plasma membrane proteins topologically oriented toward the
410 cytosol. However, if BiP:sfGFP:HDEL were within a small membrane-bound ER compartment,
411 it could not interact with a cytosolically oriented ligand. To test this, we co-expressed
412 BiP:sfGFP:HDEL with a plasma membrane-tethered GFP nanobody fused to RFP (referred to
413 as morphotrap$_{Int,}$) (Harmansa et al., 2017)). The GFP nanobody in morphotrap$_{Int}$ faces the
414 cytosol, even when tethered to membranes, allowing it to interact only with cytosolic
415 BiP:sfGFP:HDEL. Given that the morphotrap$_{Int}$ is localized to the plasma membrane, it should
416 cause the relocation of cytosolic BiP:sfGFP:HDEL, but not luminal BiP:sfGFP:HDEL. Second,
417 since a membrane-tethered nanobody is likely to have slower diffusion than the putatively
418 cytosolic BiP:sfGFP:HDEL, morphotrap$_{Int}$ co-expression would be predicted to reduce cytosolic
419 BiP:sfGFP:HDEL dynamics, but not luminal BiP:sfGFP:HDEL dynamics (**Figure 10A**).
420
421 First, we blinded our samples and categorized control and *Atlastin* mutants as "No
422 phenotype", "Partial loss" and "Complete loss", as we had done previously (**Figure 6C**). We
423 found that *Atlastin* mutants co-expressing morphotrap$_{Int}$ and BiP:sfGFP:HDEL had 47% of NMJs
424 with partial loss, 3% with complete loss, and 50% with no phenotype (**Figure 10B**). This
425 redistribution is consistent with morphotrap$_{Int}$ binding and relocalizing cytosolic

426 BiP:sfGFP:HDEL. Interestingly, rather than accumulating at the plasma membrane, the overall
427 levels of BiP:sfGFP:HDEL were reduced, suggesting that the displaced protein is targeted for
428 degradation (**Figure 10C**). Further, the reduction in partial and complete loss phenotypes
429 compared to BiP:sfGFP:HDEL expression alone (**Figure 6C vs 10B**) indicates that sequestering
430 BiP:sfGFP:HDEL at the plasma membrane uncovers residual ER networks masked by the
431 diffuse cytoplasmic signal. To test the specificity of this effect, we co-expressed
432 BiP:sfGFP:HDEL with RFP:mCD8, which has the same protein domain composition as
433 morphotrap$_{Int}$ but lacks the GFP nanobody. BiP:sfGFP:HDEL levels were unaffected in those co-
434 expressing RFP:mCD8 in *Atlastin* mutants and controls. We also found that 42% of NMJs had
435 partial loss, 50% had complete loss, and 8% had no phenotype (**Figure 10B**), similar to what we
436 observed when only BiP:sfGFP:HDEL was overexpressed in *Atlastin* mutants (**Figure 6C**). By
437 contrast, in wild-type controls, co-expression of BiP:sfGFP:HDEL with either morphotrap$_{Int}$ or
438 mCD8:RFP did not result in any relocalization of BiP:sfGFP:HDEL. Our results suggest that
439 BiP:sfGFP:HDEL protein at presynaptic terminals is displaced to the cytosol and binds to
440 morphotrap$_{Int}$ in *Atlastin* mutants, leading to its altered distribution and removal.
441
442 Next, we performed a FRAP experiment to test the dynamics of BiP:sfGFP:HDEL in the
443 presence of morphotrap$_{Int}$. First, we examined the dynamics of morphotrap$_{Int}$ itself following
444 photobleaching. We found that morphotrap$_{Int}$ had very slow recovery and plateaued at 20% in
445 wild-type and 17% in *Atlastin* mutants (**Figure 10D-E**). We hypothesized that the slow diffusion
446 of morphotrap$_{Int}$ would restrict the movement of any cytosolic BiP:sfGFP:HDEL in *Atlastin*
447 mutants. Indeed, we found that wild-type expressing morphotrap$_{Int}$ and BiP:sfGFP:HDEL had a
448 mobile fraction of 57%, while *Atlastin* mutants had a mobile fraction of 38% (**Figure 10F**). By
449 contrast, in *Atlastin* mutants co-expressing BiP:sfGFP:HDEL and non-membrane-targeted
450 RFP:mCD8, NMJs with partial loss had a mobile fraction of 51%, and those with complete loss
451 had a plateau of 66% (**Figure 9**). We hypothesize that the reduction in the mobile fraction in the
452 presence of morphotrap$_{Int}$ results from the binding of BiP:sfGFP:HDEL in the cytosol to
453 morphotrap$_{Int}$ in *Atlastin* mutants. There was a minor decrease to 57% in wild-type larvae co-
454 expressing BiP:sfGFP:HDEL and morphotrap$_{Int}$, while those co-expressing BiP:sfGFP:HDEL
455 with RFP:mCD8 plateaued at 66%. These results suggest the presence of a small cytosolic
456 population of BiP:sfGFP:HDEL in controls. Finally, we examined the recovery kinetics of
457 BiP:sfGFP:HDEL in larvae co-expressing morphotrap$_{Int}$. We found the recovery in controls is
458 slower, with a half-life of 53.23 s, while *Atlastin* mutants had a faster recovery with a half-life of

459 45.76 s. The faster half-life in *Atlastin* mutants could reflect that a small pool of BiP:sfGFP:HDEL
460 remains mobile, perhaps contained within a discontinuous section of the ER. Our findings
461 provide multiple lines of evidence that BiP:sfGFP:HDEL is displaced from the ER lumen to the
462 cytosol in *Atlastin* mutants, potentially reflecting disruption to ER integrity and function at
463 presynaptic terminals.
464
465 **Discussion**
466
467 This study revealed the architecture and dynamic behaviors of *Drosophila* neuronal ER
468 networks through a super-resolution *in vivo* imaging approach that can be adapted to visualize
469 fluorescently labeled proteins at high resolution in any larval tissue. Using this approach, we
470 provided the first characterization of presynaptic ER network dynamics *in vivo*, establishing a
471 foundation for investigating the functional significance of structural rearrangements of the ER.
472 Our analysis of *Atlastin* mutants uncovered an unexpected phenotype: while these mutants
473 maintain largely intact ER networks with only minor defects in dynamics, they exhibit
474 displacement of luminal ER proteins to the cytosol of presynaptic terminals but not in other
475 neuronal regions. These findings reveal that Atlastin serves distinct, synapse-specific functions
476 in maintaining both ER structure and function, providing mechanistic insight into the synaptic
477 deficits previously observed in *Atlastin* mutants.
478
479 **ER network dynamics at presynaptic terminals**
480
481 We observed three categories of ER dynamics at presynaptic terminals: (1) budding and
482 fusion of vesicular structures, (2) ER tubule dynamics, and (3) dynamics of foci that are retained
483 within the ER network. Disruptions in these dynamics, as seen in *Atlastin* mutants, could impair
484 synaptic signaling and contribute to neurodegenerative diseases linked to ER dysfunction. ER
485 network dynamics may depend on Atlastin-mediated ER tubule tethering and fusion to distribute
486 lipids and ER membrane proteins throughout the network to ensure proper distribution and
487 prevent fragmentation. Future work is needed to examine the specific functions of these
488 dynamics at presynaptic terminals, but we speculate below on some potential roles:
489
490 First, ER-derived vesicles could act as localized calcium signaling hubs (Burgoyne et al.,
491 2015) or serve as sites for compartmentalized local translation if they carry ribosomes (Carter et

492 al., 2020; Deng et al., 2021). The synaptic ER vesicle-like structures we observed are unlikely
493 to be involved in the secretory pathway or ER-phagy (Chino and Mizushima, 2020) because we
494 observe these vesicles re-fusing with the ER. We speculate the ER-derived vesicles observed
495 may be REEP1-4 positive, which regulates ER vesicle formation in mammalian cells (Shibata et
496 al., 2024). Notably, while overexpression of Atlastin can regulate REEP1-4 vesicle fusion, it is
497 not essential for vesicle formation. Second, ER tubule dynamics may play multiple roles, such
498 as maintaining the tension of the ER network (Espadas et al., 2019; Niu et al., 2019) and forming
499 ER-organelle contacts (Friedman et al., 2011; Hoyer et al., 2018; Rowland et al., 2014). ER
500 contacts occur at the tips and edges of ER tubules, and they have diverse functions, such as
501 promoting mitochondrial and endosome fission (Friedman et al., 2011; Hoyer et al., 2018;
502 Rowland et al., 2014). To understand how these functions are regulated at presynaptic terminals,
503 future studies could examine ER tubule interactions with other organelles using co-localization
504 experiments or ER-organelle sensors. Finally, we identified foci dynamics within ER networks.
505 We hypothesize that foci emerge due to changes in the dynamics of protein clusters at the ER
506 membrane or within the lumen. Foci dynamics occur at higher levels with the luminal ER marker
507 in contrast to the ER membrane marker. This differential distribution suggests distinct
508 organizational principles for luminal versus membrane proteins in presynaptic ER.
509
510 **Distinct Membrane and Luminal ER Phenotypes in *Atlastin* Mutants Suggest Local Stress**
511 **Responses**
512 Using the membrane marker tdTomato:Sec61β, we discovered that *Atlastin* mutants
513 have robust ER networks at presynaptic terminals. The relatively mild structural phenotypes
514 stand in sharp contrast to the diffuse distribution we and others observe for the luminal marker
515 BiP:sfGFP:HDEL, and argue against excessive ER fragmentation in *Atlastin* mutants. Despite
516 being the sole Atlastin homolog in flies, we found that loss of Atlastin causes surprisingly subtle
517 changes in ER structure and dynamics. However, we did observe specific defects with our FRAP
518 experiments, which revealed *Atlastin* mutants have discontinuous ER networks. The subtle
519 nature of these defects also suggests that other proteins may partially compensate for Atlastin's
520 function in maintaining ER structure and dynamics at presynaptic terminals.
521
522 Considering the distinct phenotypes displayed by luminal and membrane ER markers,
523 which one best represents the *Atlastin* mutant phenotype in the absence of a marker? We favor
524 the hypothesis that the true *Atlastin* ER phenotype is more likely to be similar to the

525 tdTomato:Sec61β distribution, for the following reasons: (1) tdTomato:Sec61β-expressing
526 animals still show Atlastin-associated functional defects such as defective synaptic growth,
527 indicating that Atlastin-dependent ER functions are disrupted without dramatic defects in ER
528 structure; (2) The BiP:sfGFP:HDEL phenotype becomes progressively more severe throughout
529 larval development, suggesting this marker's displacement is a secondary effect rather than a
530 direct reflection of ER architecture. Future studies in other ER-shaping mutants should examine
531 both ER membrane and ER lumen markers, as specific defects could affect one and not the
532 other, as we observed in *Atlastin* mutants.

533 Why, then, might *Atlastin* mutants displace luminal proteins to the cytosol? A key
534 observation that constrains possible mechanisms is that this displacement occurs specifically at
535 presynaptic terminals - the luminal ER marker remains properly localized in cell bodies, axons,
536 and other cell types such as muscles. This spatial specificity argues against several potential
537 global mechanisms: First, overall disruption of ER integrity seems unlikely to explain the
538 phenotype; while *Atlastin* mutants show reduced levels of the ER membrane marker Sec61β
539 and altered network structure at presynaptic terminals, catastrophic loss of ER membrane
540 integrity would likely release calcium and other ER components into the cytosol, which would be
541 incompatible with cell survival (Wang et al., 2011). Second, general defects in protein
542 translocation are unlikely, since these would affect all neuronal compartments, especially the
543 cell body where most protein translation occurs (Glock et al., 2021; McKibbin et al., 2012). Third,
544 we found no evidence for apoptosis-induced ER permeability, as *Atlastin* mutant neurons lack
545 the characteristic debris observed after neuronal death at the NMJ (Aponte-Santiago et al., 2020;
546 Graf et al., 2011).

547 Instead, the presynaptic specificity suggests more localized mechanisms. One possibility
548 is compartment-specific activation of ER stress responses like UPR (Untranslated Protein
549 Response), ERAD (ER-associated degradation) or ERCYS (ER-to-cytosol signaling)
550 (Christianson et al., 2023; Igbaria et al., 2019; Lajoie and Snapp, 2020; Read and Schröder,
551 2021; Sicari et al., 2021; Wu and Rapoport, 2018). These pathways can actively transport
552 luminal proteins to the cytosol through distinct mechanisms: in UPR and ERAD, proteins are
553 targeted for proteasomal degradation, while in ERCYS, they can acquire novel functions in the
554 cytosol. Previous work has shown that *Atlastin* mutants and other HSP-linked genes have
555 activated UPR (Lai et al., 2014; O'Sullivan et al., 2012; Zhao et al., 2016). In the case of our

556 overexpressed BiP:sfGFP:HDEL marker, either pathway could explain its accumulation in the
557 cytosol. If UPR or ERAD is activated, BiP:sfGFP:HDEL might be continuously displaced from
558 the ER but accumulate when the proteasome cannot keep up with its degradation. Alternatively,
559 if ERCYS is activated, BiP:sfGFP:HDEL might accumulate in the cytosol as part of a regulated
560 signaling response. We cannot distinguish between these possibilities, but multiple lines of
561 evidence support the general activation of ER stress pathways in *Atlastin* mutants. First, the
562 phenotype progresses from 1st to 3rd instar larvae, consistent with gradually activated stress
563 responses. Second, synaptic terminals show a specific reduction in Sec61β levels, suggesting
564 local defects in protein homeostasis. Given these observations, what might trigger an ER stress
565 response in *Atlastin* mutants? The underlying mechanism remains to be determined, but the
566 progressive nature of the phenotype and the eventual failure of luminal ER protein retention
567 suggest a gradual deterioration of ER homeostasis at synaptic terminals. Future work will be
568 needed to identify the specific cellular changes that initiate this stress response.
569

570 **ER network structure and function are compartmentalized across neuronal regions**

571 Our findings reveal distinct requirements for Atlastin across neuronal regions. At
572 presynaptic terminals, loss of Atlastin leads to the displacement of luminal proteins and reduced
573 levels of Sec61β. This reduction in Sec61β suggests other ER membrane proteins, such as ER
574 tethers, could also be affected, potentially disrupting ER-dependent processes like endosome
575 trafficking that rely on proper ER-organelle contacts. This reduction in Sec61β mirrors findings
576 in *Drosophila* null mutants of Reticulon-1, another ER shaping and HSP-linked gene, in which
577 levels of STIM and Stukorf are also decreased on ER tubules (Pérez-Moreno et al., 2023). Yet,
578 a key distinction emerges as Reticulon-1 null mutants maintain normal luminal ER protein
579 localization, suggesting unique features of *Atlastin* mutant ER networks. These region-specific
580 phenotypes highlight fundamental differences in ER organization and function across neuronal
581 regions. Further evidence for neuronal ER compartmentalization comes from studies of
582 mammalian spinal axons, where Atlastin-fusion incompetent mutants showed ladder-like ER
583 expansion (Zhu et al., 2022). We observed similar ladder-like structures with three-way junctions
584 in both control and *Atlastin* mutant axons labeled with tdTomato:Sec61β, indicating that Atlastin
585 is not solely responsible for ER tubule fusion in axons. This neuronal-specific organization
586 contrasts with the long, unbranched ER tubules found in Atlastin-deficient Hela or Cos-7 cells
587 (Hu et al., 2009; Niu et al., 2019), suggesting neurons possess unique compensatory tubule-

588 fusion machinery. Future work should comprehensively examine the common and unique
589 defects associated with HSP gene dysfunction across neuronal compartments.

590 **Methods**

591

592 *Drosophila* stocks

593 *Drosophila melanogaster* was cultured on a standard medium at 22–25°C. Detailed genotypes
594 and sexes used for experiments are described in Table S1. Stocks used in this study
595 include: Vglut-Gal4 (Bloomington *Drosophila* Stock Center (BDSC_24635), BG57-Gal4 (gift
596 from Vivian Budnik), *atl*^{2} (gift from James McNew), third chromosome deficiency (BDSC_7948),
597 UAS-BiP:sfGFP:HDEL (BDSC_64748), 20XUAS-tdTomato:Sec61β (BDSC_64746), UAS-
598 CD8:RFP (BDSC_27391) and UAS-morphotrap$_{Int}$ (gift from Chi-Kuang Yao).

599

600 Live imaging of luminal and membrane ER markers

601 1st and wandering 3rd instar larvae were dissected in Ca^{2+}-free HL3.1 (Feng et al., 2004) and
602 axons were severed from the central nervous system. Dissections were performed in the live
603 imaging slide described below. Larvae were imaged at room temperature with a 63X (n.a. 1.4)
604 oil immersion objective, using an Airyscan LSM 880 microscope in super-resolution mode and
605 Zen Black software. Raw image stacks were processed in Zen Blue or Zen Black using 3D
606 Airyscan processing with automatic settings.

607

608 For 3rd instar larvae, Z-stacks of soma clusters, axons or presynaptic type Ib terminals at muscle
609 4 in segment A5 (unless otherwise noted) were acquired to measure the levels of luminal ER
610 markers, to categorize ER network phenotypes, or for morphological measurements. For 1st
611 instar larvae, live larval fillets were stained with 1:250 dilution of 1.5 mg/ml HRP Alexa Fluor 647
612 (Jackson ImmunoResearch) in HL3.1 for 5 min followed by a 1 min wash. Next, Z-stacks of 1st
613 instar presynaptic terminals at muscle 4 in segment A3-A5 were acquired and used to categorize
614 ER network phenotypes.

615

616 To record the dynamics of the luminal ER marker BiP:sfGFP:HDEL, 16-bit Z-stacks of a single
617 bouton (8 slices with 0.5 micron spacing) were collected for 100 frames at a frame rate of 0.73
618 seconds/stack. To record ER dynamics with the membrane ER marker tdTomato:Sec6β, 8-bit

619 Z-stacks of a single bouton (20 slices with 0.1850 micron spacing) were collected for 60 frames
620 at a frame rate of 0.92 seconds/stack.
621
622 Construction of *in vivo* imaging slide for *Drosophila* larvae
623 To make the reusable imaging slide, Press-To-Seal Silicone Isolators (Grace Bio-labs; CQS-
624 13R-2.0) were mounted onto rectangular glass slides, which then were filled from their centers
625 to their tops with Krayden Dow Sylgard 184 Silicone (Thermo Fisher Scientific). Each slide with
626 a Press-To-Seal Silicone Isolator was leveled to ensure the silicone cured evenly at room
627 temperature. Minutien pins (Fine Science Tools) were cut with nail clippers and used to stretch
628 the larvae and fix it in place. Pins were pressed into the cured Sylgard 184 Silicone and a few
629 drops of hemolymph-like solution HL3.1 were added. Next, a coverslip was placed on top of the
630 dissected larvae, each corner was gently pressed down, and excess HL3.1 was removed with a
631 Kimwipe, thus sealing the coverslip to the silicone isolator.
632
633 Fixed tissue staining
634 Wandering 3rd instar larvae were dissected in Ca^{2+}-free HL3.1 and fixed for 17 min in Ca^{2+}-free
635 HL3.1 containing 4% PFA. Larvae were blocked and permeabilized overnight in PBS containing
636 0.25% Saponin, 2.5% normal goat serum (NGS), 2.5% bovine serum albumin (BSA), and 0.1%
637 sodium azide. Fixed larvae (**Figure 3**) were stained with 1:500 FluoTag®-X4 anti-RFP (#N0404,
638 Nanotag Biotechnologies) at 4°C for 24 hrs and with 1:100 HRP Alexa Fluor 647 at room
639 temperature for 2hrs. Stained larvae were mounted in ProLong Diamond Antifade Mountant
640 (#P36970; Thermo-Fisher Scientific, Waltham, MA, USA). Z-stacks were collected of *Drosophila*
641 larval NMJs in muscle 4 of segment A5 at room temperature on a Nikon Ni-E upright microscope
642 equipped with 100x (n.a. 1.45) oil immersion objective, a Yokogawa CSU-W1 spinning-disk
643 head, and an Andor iXon 897U EMCCD camera. Images were collected using Nikon Elements
644 AR software.
645
646 FRAP experiment
647
648 Imaging was conducted using a Nikon super-resolution spinning disk SoRA system in W1-
649 spinning disk mode, equipped with an Apo 60x Oil DIC N2 objective and set to a 12-bit depth.
650 We photobleached boutons in the middle of a synaptic branch to ensure BiP:sfGFP:HDEL could
651 recover from both the top and bottom of the photobleached region. To capture the rapid recovery

652 of BiP:sfGFP:HDEL, we imaged a single slice of NMJs at muscle 4 and sequentially acquired
653 488 and 561 channels with an exposure time of 100ms. For all NMJs, we photobleached single
654 boutons within a 6.8x7.8 microns region in the middle of neuronal branch. Each movie acquired
655 used an ND sequence acquisition consisting of three phases: (1) we acquired five frames at
656 maximum speed (100Mhz) before photobleaching; (2) we photobleached BiP:sfGFP:HDEL and
657 RFP:mCD8 or morphotrap$_{Int}$ using a 405 nm depletion laser with a dwell time of 100µs for a
658 duration of 2s; and (3) we imaged the recovery of both BiP:sfGFP:HDEL and RFP:mCD8 or
659 morphotrap$_{Int}$ with a 10s interval for 2 minutes for experiments in **Figure 9** and 5 minutes for
660 experiments in **Figure 10**.
661
662 Digitonin experiments
663 Digitonin experiments were conducted in live fillets from larvae expressing the luminal ER
664 marker, UAS-BiP:sfGFP:HDEL, under the control of the neuronal driver Vglut-GAL4. Fillets were
665 stained with 1:500 1.5 mg/ml HRP Alexa Fluor 594 (Jackson ImmunoResearch) or 1:250 HRP
666 Alexa Fluor 647 in HL3.1 for 5 min, followed by a 1 min HL3.1 wash. Next, pre-digitonin Z-stacks
667 were acquired from muscle 4 NMJs from segments A3 to A5 (both hemisegments) using the
668 spinning disk confocal microscope described above. Fillets were subsequently incubated with
669 0.05% digitonin in HL3.1 for 5 min, then rinsed with HL3.1 and re-incubated with HRP Alexa
670 Fluor 594 or HRP Alexa Fluor 647 for 5 min. Preps were then washed for 1 min with HL3.1.
671 Finally, post-digitonin Z-stacks were acquired of the same NMJs.
672
673 Image analysis
674 Debris, axons, and large fluorescent aggregates (sometimes observed for tdTomato:Sec61β)
675 were manually removed from all images before analyses of maximum projections or Z-stacks.
676 Neuronal masks were created by first conducting a background subtraction of the image (rolling
677 ball, 50 pixel radius), and then introducing a gaussian blur before thresholding using Otsu or Li
678 algorithms. For live image analysis, maximum intensity projections of each timepoint were
679 corrected for (1) photobleaching using histogram matching and (2) sample drift or muscle
680 contraction using the StackReg plugin (Thevenaz et al., 1998).
681
682 *Presynaptic levels of ER membrane* marker tdTomato:Sec61β *(**Figure 3**)*: *A* custom FIJI macro
683 consisting of the following steps was employed on maximum intensity projections,: (1) An NMJ
684 mask was created using the α-HRP neuronal marker; (2) The integrated density of the ER

685 membrane marker tdTomato:Sec61β was measured within the α-HRP mask; (3) The mean
686 intensity of the ER membrane marker at presynaptic terminals was calculated by dividing the
687 tdTomato:Sec61β integrated density by the area of the presynaptic terminal.
688
689 *Analysis of NMJ morphology:* Satellite and total bouton numbers were manually counted from
690 blinded maximum intensity projections of fixed and α-HRP labeled larvae. Satellite boutons were
691 defined as any string of 5 or fewer boutons extending from the main axis of the NMJ.
692
693 *Categorization of ER dynamics:* For dynamics analysis, we used the same dataset as the control
694 in **Figure 2**, **Figure 5**, and **Figure 5_Supplement**. Maximum intensity projection timelapse
695 movies were blinded and replayed 3-4 times before categorization. We identified three distinct
696 categories of ER dynamics in presynaptic terminals of *Drosophila* motor neurons (note that a
697 single bouton can exhibit multiple types of dynamics): (1) **ER budding** – small vesicle-like
698 structures emerging from the ER network and re-fusing in a different region; (2) **ER tubule**
699 **dynamics**, encompassing four subcategories as follows: (a) Tubule displacement, involving
700 tubules that changed their localization within boutons without detaching from the ER network;
701 (b) Tubule extension, where an ER tubule emerged and extended from the ER network; (c)
702 Tubule retraction, characterized by the retraction and disappearance of an ER tubule from the
703 ER network; and (d) Tubule extension and retraction, indicating an ER tubule both extending
704 and retracting from the ER network within the timelapse. (3) **Foci dynamics** – round, bright
705 puncta moving within the ER network and (4) **static** – boutons that lacked observable dynamics.
706
707 *Presynaptic levels of luminal ER proteins at* Drosophila *motor neurons:* A custom FIJI macro
708 consisting of the following steps was employed on Z-stacks: (1) We created an NMJ mask using
709 the luminal ER protein marker. (2) Using this mask, we measured the neuron volume and the
710 integrated density of the marker. (3) We calculated the mean intensity of the marker by dividing
711 the integrated density by the volume of the presynaptic terminal.
712
713 *Categorization of luminal ER marker distribution:* Images were blinded before analysis to ensure
714 unbiased qualitative analysis of luminal ER marker BiP:sfGFP:HDEL in controls and *Atlastin*
715 mutants. Maximum intensity projections were then sorted into three phenotypic categories: (1)
716 **"Partial loss"** - luminal ER marker localizes to ER networks but is partially displaced to the
717 cytosol, (2) **"Complete loss"** - luminal ER marker mostly displaced to the cytosol and ER

718 networks are not detectable, and (3) **<u>"No phenotype"</u>** - luminal ER marker completely localizes
719 to ER networks.
720
721 *Presynaptic levels of cytosolic or luminal ER proteins pre- and post-digitonin treatment*: Images
722 were blinded and maximum projections were created for further analysis. Neuronal outlines were
723 obtained by manually tracing the α-HRP-positive region in FIJI. Next, the integrated density of
724 UAS-GFP or UAS-BiP:sfGFP:HDEL was quantified within the manually traced neuronal outlines.
725 Mean intensity was calculated by dividing the integrated density by the area of the presynaptic
726 terminal.
727
728 *BiP:sfGFP:HDEL levels before and after photobleaching*: Images were blinded for analysis. The
729 20 frames corresponding to the photobleaching event were removed since this prevented the
730 Stackreg plugin from working correctly. Movies with uncorrectable drift were excluded. For the
731 analysis, we drew 3 ROIs corresponding to the region that was photobleached, a region away
732 from the bleach site and the background. A Fiji macro was then used to measure the mean
733 intensities at these 3 regions per movie. The mean intensities at the site of photobleaching of
734 BiP:sfGFP:HDEL, RFP:mCD8 or morphotrap$_{Int}$ were background subtracted and normalized to
735 the mean intensity of the non-bleached region. We also used the same approach to measure
736 the levels of BiP:sfGFP:HDEL before FRAP (**Figure 10C**).
737
738 <u>Statistics</u>
739 GraphPad Prism software was used to perform statistical analyses and generate graphs.
740 Statistical analyses were conducted using parametric tests (e.g. one-way ANOVA, Student's t-
741 test) for normally distributed data, and non-parametric tests (e.g. Kruskal-Wallis, Mann-Whitney
742 tests) if the data was not normally distributed. Chi-squared tests were used for categorical data.
743 p-values were set to *<0.05, **<0.01, ***<0.001.
744
745 **Acknowledgements**
746 We thank the Bloomington *Drosophila* Stock Center (Indiana University, Bloomington, IN, NIH
747 P40OD018537) and James McNew for fly lines, Steve Del Signore for help with image analysis,
748 and Bruce Goode for use of the SoRA microscope. We also thank Chi-Kuang Yao for sharing
749 reagents and stimulating discussion. This work was supported by NINDS grants R01 NS103967
750 to A.A.R., and T32 007292 and K99 NS136720-02 to M.C.Q.F.

751

752 **Figure legends:**

753

754 **Figure 1. *In vivo* imaging of ER networks in *Drosophila* motor neurons.** (**A**) The schematic
755 setup for live imaging experiments in this study consists of a glass microscope slide with a
756 mounted silicone isolator filled with Sylgard. Small metal pins were used to stretch the larvae
757 (small round dots). Finally, a coverslip was placed on top of the larval fillet for imaging with an
758 oil objective on upright or inverted microscopes. (**B**) A representative single slice of an Airyscan
759 microscopy Z-stack of the center (top) or periphery (bottom) of the cell body of a motor neuron
760 expressing the luminal ER marker BiP:sfGFP:HDEL. Pink dotted boxes indicate ER tubules and
761 sheets. (**C**) Maximum projections of Z-stacks acquired with an Airyscan microscope of two
762 different motor neuron axons expressing the luminal ER marker BiP:sfGFP:HDEL. (**D**)
763 Representative maximum projection of a Z-stack acquired with an Airyscan microscope of a
764 motor neuron presynaptic terminal expressing the luminal ER marker BiP:sfGFP:HDEL. The
765 magenta outline highlights the neuronal boundary. Arrows indicate boutons containing ER
766 baskets or ladder-like ER structures.

767

768 **Figure 2. Dynamics of luminal and membrane ER markers at presynaptic terminals.** (**A**)
769 Diagram of a presynaptic terminal of *Drosophila* motor neurons highlighting *en passant* and
770 terminal boutons with the ER in grey. (**B**, **top**) Maximum intensity projection of Airyscan Z-stacks
771 from the beginning (t=0) and the end (t=39 sec) of a timelapse movie (**Movie S1**) of a single
772 wild-type bouton expressing the ER membrane marker tdTomato:Sec61β. (**B, bottom**)
773 Magnification of the region in the dotted red box of dynamics observed from 0 sec to 1.4 sec of
774 the movie. (**C, top**) Maximum intensity projection of Airyscan Z-stacks from the beginning (t=0)
775 and the end (t=72 sec) of a timelapse movie (**Movie S4**) of a single wild-type bouton expressing
776 the luminal ER marker BiP:sfGFP:HDEL. (**C, bottom**) Magnification of the region in the dotted
777 red box of dynamics observed from 0 sec to 1.4 sec of the movie. (**D**) Presynaptic terminals
778 exhibiting ER budding, focus dynamics and various types of ER tubule dynamics (ER tubule
779 displacement, tubule extension, and tubule retraction). (**E**) Qualitative categorization of the
780 percentage of *en passant* and terminal boutons that are dynamic or static expressing the ER
781 membrane marker tdTomato: Sec61β. (**F**) Qualitative categorization of the percentage of
782 dynamic terminal boutons expressing the ER membrane marker tdTomato:Sec61β that exhibit
783 ER budding, foci dynamics or ER tubule dynamics. (**G**) Qualitative categorization of the

784 percentage of dynamic terminal boutons expressing the ER membrane marker
785 tdTomato:Sec61β that exhibit tubule displacement, tubule extension, tubule retraction and both
786 tubule extension and retraction. The same control dataset used in E-G was used in **Figure 5**,
787 and **Figure 5_Supplement**.
788
789 **Figure 3. *Atlastin* mutants have lower levels of the ER membrane tdTomato: Sec61β at**
790 **presynaptic terminals.** (**A**) Representative maximum intensity projection of a spinning disk
791 confocal Z-stack from fixed larvae expressing the ER membrane marker tdTomato:Sec61β
792 (black) in control (**left**) and *Atlastin* mutants (**right**). The neuronal outline (derived from the α-
793 HRP mask) is shown in magenta. (**B**) Quantification of satellite boutons normalized to total
794 bouton number in control and *Atlastin* mutants. (**C**) Quantification of the intensity of the ER
795 membrane marker tdTomato:Sec61β, normalized to wild-type control. (**D**) Coefficient of variation
796 (CoV) of the ER membrane marker tdTomato:Sec61β. (**B-D**) Graphs show mean +/- s.e.m. from
797 30 control and 30 *Atlastin* mutant NMJs.
798
799 **Figure 3 – Figure Supplement. *Atlastin* mutants expressing the ER membrane**
800 **tdTomato:Sec61β exhibit robust ER networks at presynaptic terminals.** (**A, B**)
801 Representative maximum projection of a Z-stack acquired live by Airyscan microscopy of control
802 and *Atlastin* mutant NMJs expressing the ER membrane marker tdTomato: Sec61β at
803 presynaptic terminals. These images are not contrast matched because *Atlastin* mutants exhibit
804 lower levels of the tdTomato:Sec61β (See **Figures 3C**).
805
806 **Figure 4. *Atlastin* mutants expressing the ER membrane tdTomato:Sec61β in axon**
807 **bundles and soma clusters have distinct phenotypes.** (**A**) Representative middle slice of
808 axon bundles in control (top) and *Atlastin* mutants (bottom) expressing tdTomato:Sec61β. (**B**)
809 Representative top or middle slices of somas in control (top) and *Atlastin* mutants (bottom)
810 expressing tdTomato:Sec61β. (**C,F**) Quantification of the intensity of the ER membrane marker
811 tdTomato:Sec61β. (**D,G**) Quantification of the area of the ER membrane marker
812 tdTomato:Sec61β. (**E,H**) Coefficient of variation (CoV) of the ER membrane marker
813 tdTomato:Sec61β. For axon bundles, graphs show mean +/- s.e.m. from 29 control and 32
814 *Atlastin* mutant NMJs. For soma clusters, graphs show mean +/- s.e.m. from 26 control and 33
815 *Atlastin* mutant NMJs.

816

817 **Figure 5. *Atlastin* mutants have mild ER dynamics phenotypes.** (**A**) Representative images
818 of terminal (left) or *en passant* (right) boutons in controls (top) and *Atlastin* mutants (bottom)
819 (**Movies S7-14**). (**B**) Percentage of dynamic versus static boutons in controls and *Atlastin*
820 mutants expressing the ER membrane marker tdTomato:Sec61β, analyzed separately for
821 terminal and *en passant* boutons. Terminal bouton analysis included 75 control (65 dynamic, 10
822 static) and 83 *Atlastin* mutant boutons (63 dynamic, # static). *En passant* bouton analysis
823 included 29 control (11 dynamic, 18 static) and 36 *Atlastin* mutant boutons (11 dynamic, 25
824 static). (**C**) Distribution of ER dynamic types (budding, foci dynamics, or ER tubule dynamics) in
825 dynamic terminal boutons expressing tdTomato:Sec61β. (**D**) Distribution of ER dynamics types
826 in dynamic *en passant* boutons expressing tdTomato:Sec61β. Dynamic boutons were further
827 analyzed in **Figure 5_Supplement**. Data from control animals were also used in **Figure 2** and
828 **Figure 5_Supplement**.

829

830 **Figure 5 – Supplement.** (**A**) A qualitative categorization of the percentage of dynamic terminal
831 boutons in controls and *Atlastin* mutants expressing the ER membrane marker
832 tdTomato:Sec61β that exhibit tubule displacement, tubule extension, tubule retraction, and both
833 tubule extension and retraction. (**B**) A qualitative categorization of the number of dynamic
834 categories per terminal bouton in control and *Atlastin* mutants. The same control and *Atlastin*
835 mutant dataset were used in **Figure 2**, and **Figure 5**.

836

837 **Figure 6. Luminal ER proteins are displaced to the cytosol in *Atlastin* mutants.** Maximum
838 projection of a Z-stack acquired live with an Airyscan microscope of control (**A**) and *Atlastin*
839 mutant (**B**) NMJs expressing the ER lumen marker BiP:sfGFP:HDEL. (**B**) *Atlastin* mutants exhibit
840 two distinct phenotypes at presynaptic terminals that were categorized as partial loss (**B, top**) or
841 complete loss (**B, bottom**). Control and *Atlastin* mutant images are contrast matched. (**C**) A
842 qualitative categorization of presynaptic terminals in control and *Atlastin* mutants exhibiting
843 "partial loss", "complete loss" or "no phenotype". (**D**) Histogram of normalized mean intensities
844 of the ER lumen marker BiP:sfGFP:HDEL. Displacement does not strongly correlate with steady-
845 state levels of BiP:sfGFP:HDEL. (**E**) Quantification of the intensity of the luminal ER marker
846 BiP:sfGFP:HDEL. (**F**) Coefficient of variation (CoV) of the luminal ER marker BiP:sfGFP:HDEL
847 in neurons of control and *Atlastin* mutant. (**E, F**) Graphs show mean +/- s.e.m. from 8 control
848 and 15 *Atlastin* mutant NMJs.

849

850 **Figure 6 – Supplement. Is and Ib motor neurons in various muscles and abdominal**
851 **segments of 3rd instar *Atlastin* mutant larvae exhibit similar cytosolic displacement of**
852 **BiP:sfGFP:HDEL.** Maximum projection of a live Airyscan Z-stack from larvae expressing the
853 ER lumen marker BiP:sfGFP:HDEL at muscles 12-13 (**A, left**), muscles 6-7 (**A, right**), muscle 4
854 in segment A2 (**B, left**) and muscle 4 in segment A4 (**B, right**).

855

856 **Figure 7. Luminal ER proteins are not displaced in other neuronal compartments or cell**
857 **types in *Drosophila* 3rd instar larvae.** All images were acquired by live Airyscan microscopy
858 from larvae expressing the ER lumen marker BiP:sfGFP:HDEL with Vglut-GAL4 (motor neurons)
859 or BG57-GAL4 (body wall muscles). (**Left panel**) Maximum projection of a Z-stack of motor
860 neuron axons. (**Middle panel**) A single slice of motor neuron cell bodies. (**Right panel**) A single
861 slice of body wall muscles.

862

863 **Figure 8. The luminal displacement phenotype in *Atlastin* mutants is progressive.** (**A, B**)
864 Maximum intensity projections of a live Airyscan Z-stack acquired of 1st instar larvae expressing
865 the ER lumen marker BiP:sfGFP:HDEL (black) with a neuronal outline (magenta, derived from
866 the α-HRP mask) in control (A) and *Atlastin* mutants (B). (**C**) A qualitative categorization of
867 presynaptic terminals in control and *Atlastin* mutant 1st instar larvae expressing the ER lumen
868 marker BiP:sfGFP:HDEL that exhibit “partial loss”, “complete loss” or “no phenotype”. Data are
869 shown from 16 control NMJs and 16 *Atlastin* mutant NMJs.

870

871 **Figure 9. FRAP analysis of BiP:sfGFP:HDEL recovery in *Atlastin* mutants.** (**A**) Diagram of
872 the recovery of BiP:sfGFP:HDEL in controls and *Atlastin* mutants with partial loss or complete
873 loss. (**B**) Representative slices from movies of controls and *Atlastin* mutants with partial loss or
874 complete loss co-expressing mCD8:RFP and BiP:sfGFP:HDEL pre-bleach, after FRAP and 2
875 min post-FRAP (**Movies S15-19**). (**C**) Mean recovery of mCD8:RFP in control (black squares)
876 and *Atlastin* mutants with partial loss (empty lime green triangles) and complete loss (green
877 triangles). (**D**) Mean recovery of BiP:sfGFP:HDEL in control (black squares) and *Atlastin* mutants
878 with partial loss (empty lime green triangles) and complete loss (green triangles). The table
879 contains the results from the non-linear fit one-phase association of the data for each dataset.
880 The s.e.m. are represented by solid lines and shading: controls (n=10) have black lines with grey

881 shading, *Atlastin* mutants with partial loss (n=6) have lime green lines and lime green shading,
882 and *Atlastin* mutants with complete loss (n= 8) have green lines with light green shading.
883
884 **Figure 10 – Supplement. Luminal ER proteins displaced to the cytosol are sensitive to**
885 **digitonin treatment.** (**A**) Maximum projections of Z-stacks acquired live with a spinning disk
886 confocal of boutons expressing with Vglut-Gal4 GFP (control 1), BiP:sfGFP:HDEL (control 2),
887 BiP:sfGFP:HDEL in *Atlastin* mutants exhibiting partial loss and BiP:sfGFP:HDEL in *Atlastin*
888 mutants exhibiting complete loss. (**B**) Diagram of the expected distribution patterns before and
889 after digitonin treatment of GFP and BiP:sfGFP:HDEL. Note that digitonin treatment causes
890 partial ER fragmentation. **(C)** Fractional change of fluorescence intensity at presynaptic
891 terminals expressing GFP (cytosolic protein) or BiP:sfGFP:HDEL in control and *Atlastin* mutants
892 following digitonin treatment. Graphs show mean +/- s.e.m. from 18 control and 20 *Atlastin*
893 mutant NMJs. Statistical significance was only calculated between BiP:sfGFP:HDEL samples
894 since the baseline fluorescence and distribution of this marker was sensitive to digitonin
895 treatment in a manner distinct from cytosolic GFP.
896
897 **Figure 10. BiP:sfGFP:HDEL in the cytosol binds morphotrap$_{Int}$ in *Atlastin* mutants.** (**A**)
898 Diagram of the recovery of BiP:sfGFP:HDEL in controls and *Atlastin* mutants co-expressing
899 morphotrap$_{Int}$. (**B**) Distribution of BiP:sfGFP:HDEL phenotypes (partial loss, complete loss, or no
900 phenotype) in control and *Atlastin* mutant presynaptic terminals co-expressing either mCD8:RFP
901 or morphotrap$_{Int}$. (**C**) Intensity of BiP:sfGFP:HDEL in control and *Atlastin* mutant terminals co-
902 expressing either mCD8:RFP or morphotrap$_{Int}$. (**D**) Representative maximum projections of
903 controls (**Movies S20-22**) and *Atlastin* mutants (**Movies S23-24**) co-expressing morphotrap$_{Int}$
904 and BiP:sfGFP:HDEL pre-bleach, after FRAP and 5 min post-FRAP. (**E**) Mean recovery of
905 mCD8:RFP in control (black squares) and *Atlastin* mutants (green triangles). (**F**) Mean recovery
906 of BiP:sfGFP:HDEL in control (black squares) and *Atlastin* mutants (green triangles). The tables
907 contain the results from the non-linear fit one-phase association equation of all the datasets. The
908 s.e.m. are represented by solid lines and shading: controls have black lines with grey shading,
909 *Atlastin* mutants have green lines with light green shading. For 10A-B, there were 27 controls
910 co-expressing BiP:sfGFP:HDEL and mCD8:RFP, 28 controls co-expressing BiP:sfGFP:HDEL
911 and morphotrap$_{Int}$, 24 *Atlastin* mutants co-expressing BiP:sfGFP:HDEL and mCD8:RFP, and 24
912 *Atlastin* mutants co-expressing BiP:sfGFP:HDEL and morphotrap$_{Int}$. For 10 E-F, there were 16

913 controls co-expressing BiP:sfGFP:HDEL and morphotrap$_{Int}$ and 19 *Atlastin* mutants co-
914 expressing BiP:sfGFP:HDEL and morphotrap$_{Int}$.
915
916
917 **Movies S1-3.** Movies acquired at a frame rate of 0.65 frames per second of presynaptic
918 terminals expressing the ER membrane marker tdTomato:Sec61β. These movies are played at
919 a frame rate of 10 frames per second and the scale bar is 1 μm.
920
921 **Movies S4-6:** Movies acquired at a frame rate of 0.73 frames per second of presynaptic
922 terminals expressing the ER membrane marker tdTomato:Sec61β. These movies are played at
923 a frame rate of 10 frames per second and the scale bar is 1 μm.
924
925 **Movie S7:** Example movie of a static proximal bouton of controls expressing the ER membrane
926 marker tdTomato:Sec61β acquired at a frame rate of 0.92 seconds/stack. The movie is played
927 at a frame rate of 5 frames per second and the scale bar is 2 μm.
928
929 **Movie S8:** Example movie of a dynamic proximal bouton of controls expressing the ER
930 membrane marker tdTomato:Sec61β acquired at a frame rate of 0.92 seconds/stack. The movie
931 is played at a frame rate of 5 frames per second and the scale bar is 2 μm.
932
933 **Movie S9:** Example movie of a static terminal bouton of controls expressing the ER membrane
934 marker tdTomato:Sec61β acquired at a frame rate of 0.92 seconds/stack. The movie is played
935 at a frame rate of 5 frames per second and the scale bar is 2 μm.
936
937 **Movie S10:** Example movie of a dynamic terminal bouton of controls expressing the ER
938 membrane marker tdTomato:Sec61β acquired at a frame rate of 0.92 seconds/stack. The movie
939 is played at a frame rate of 5 frames per second and the scale bar is 2 μm.
940
941 **Movie S11:** Example movie of a static proximal bouton of *Atlastin* mutants expressing the ER
942 membrane marker tdTomato:Sec61β acquired at a frame rate of 0.92 seconds/stack. The movie
943 is played at a frame rate of 5 frames per second and the scale bar is 2 μm.
944
945 **Movie S12:** Example movie of a dynamic proximal bouton of *Atlastin* mutants expressing the
946 ER membrane marker tdTomato:Sec61β acquired at a frame rate of 0.92 seconds/stack. The
947 movie is played at a frame rate of 5 frames per second and the scale bar is 2 μm.
948
949 **Movie S13:** Example movie of a static terminal bouton of *Atlastin* mutants expressing the ER
950 membrane marker tdTomato:Sec61β acquired at a frame rate of 0.92 seconds/stack. The movie
951 is played at a frame rate of 5 frames per second and the scale bar is 2 μm.
952

953 **Movie S14:** Example movie of a dynamic terminal bouton of *Atlastin* mutants expressing the ER
954 membrane marker tdTomato:Sec61β acquired at a frame rate of 0.92 seconds/stack. The movie
955 is played at a frame rate of 5 frames per second and the scale bar is 2 μm.
956
957 **Movie S15:** Representative movie of a control NMJ expressing mCD8:RFP pre-bleach and after
958 FRAP every 10 secs for 2 min. The movie is played at a frame rate of 5 frames per second, and
959 the scale bar is 5 μm.
960
961 **Movie S16:** Representative movie of a control NMJ expressing BiP:sfGFP:HDEL pre-bleach and
962 after FRAP every 10 secs for 2 min. The movie is played at a frame rate of 5 frames per second,
963 and the scale bar is 5 μm.
964
965 **Movie S17:** Representative movie of an *Atlastin* mutant NMJ with partial loss expressing
966 mCD8:RFP pre-bleach and after FRAP every 10 secs for 2 min. The movie is played at a frame
967 rate of 5 frames per second, and the scale bar is 5 μm.
968
969 **Movie S18:** Representative movie of an *Atlastin* mutant NMJ with partial loss expressing
970 BiP:sfGFP:HDEL pre-bleach and after FRAP every 10 secs for 2 min. The movie is played at a
971 frame rate of 5 frames per second, and the scale bar is 5 μm.
972
973 **Movie S19:** Representative movie of an *Atlastin* mutant NMJ with complete loss expressing
974 mCD8:RFP pre-bleach and after FRAP every 10 secs for 2 min. The movie is played at a frame
975 rate of 5 frames per second, and the scale bar is 5 μm.
976
977 **Movie S20:** Representative movie of an *Atlastin* mutant NMJ with complete loss expressing
978 BiP:sfGFP:HDEL pre-bleach and after FRAP every 10 secs for 2 min. The movie is played at a
979 frame rate of 5 frames per second, and the scale bar is 5 μm.
980
981 **Movie S21:** Representative movie of a control NMJ expressing morphotrap$_{int}$ pre-bleach and
982 after FRAP every 10 secs for 5 min. The movie is played at a frame rate of 5 frames per second,
983 and the scale bar is 5 μm.
984
985 **Movie S22:** Representative movie of a control NMJ expressing BiP:sfGFP:HDEL pre-bleach and
986 after FRAP every 10 secs for 5 min. The movie is played at a frame rate of 5 frames per second,
987 and the scale bar is 5 μm.
988
989 **Movie S23:** Representative movie of a *Atlastin* mutant NMJ expressing morphotrap$_{int}$ pre-bleach
990 and after FRAP every 10 secs for 5 min. The movie is played at a frame rate of 5 frames per
991 second, and the scale bar is 5 μm.
992
993 **Movie S24:** Representative movie of a *Atlastin* mutant NMJ expressing BiP:sfGFP:HDEL pre-
994 bleach and after FRAP every 10 secs for 5 min. The movie is played at a frame rate of 5 frames
995 per second, and the scale bar is 5 μm.

996 **References:**

997

998 Aponte-Santiago NA, Ormerod KG, Akbergenova Y, Littleton JT. 2020. Synaptic Plasticity
999 Induced by Differential Manipulation of Tonic and Phasic Motoneurons in *Drosophila*. *J*
1000 *Neurosci* **40**:6270–6288. doi:10.1523/JNEUROSCI.0925-20.2020
1001 Audhya A, Desai A, Oegema K. 2007. A Role for Rab5 in Structuring the Endoplasmic
1002 Reticulum. *The Journal of Cell Biology* **178**:43–56.
1003 Benedetti L, Fan R, Weigel AV, Moore AS, Houlihan PR, Kittisopikul M, Park G, Petruncio A,
1004 Hubbard PM, Pang S, Xu CS, Hess HF, Saalfeld S, Rangaraju V, Clapham DE, Camilli
1005 PD, Ryan TA, Lippincott-Schwartz J. 2024. Periodic ER-plasma membrane junctions
1006 support long-range Ca2+ signal integration in dendrites.
1007 doi:10.1101/2024.05.27.596121
1008 Blackstone C. 2018. Hereditary spastic paraplegia. *Handbook of Clinical Neurology,* **Vol.**
1009 **148**:633–651. doi:10.1016/B978-0-444-64076-5.00041-7
1010 Blackstone C. 2012. Cellular Pathways of Hereditary Spastic Paraplegia. *Annu Rev Neurosci*
1011 **35**:25–47. doi:10.1146/annurev-neuro-062111-150400
1012 Blackstone C, O'Kane CJ, Reid E. 2011. Hereditary spastic paraplegias: membrane traffic and
1013 the motor pathway. *Nat Rev Neurosci* **12**:31–42. doi:10.1038/nrn2946
1014 Boutry M, Morais S, Stevanin G. 2019. Update on the Genetics of Spastic Paraplegias. *Curr*
1015 *Neurol Neurosci Rep* **19**:18. doi:10.1007/s11910-019-0930-2
1016 Burgoyne T, Patel S, Eden ER. 2015. Calcium signaling at ER membrane contact sites.
1017 *Biochimica et Biophysica Acta (BBA) - Molecular Cell Research*, 13th European
1018 Symposium on Calcium **1853**:2012–2017. doi:10.1016/j.bbamcr.2015.01.022
1019 Carter SD, Hampton CM, Langlois R, Melero R, Farino ZJ, Calderon MJ, Li W, Wallace CT,
1020 Tran NH, Grassucci RA, Siegmund SE, Pemberton J, Morgenstern TJ, Eisenman L,
1021 Aguilar JI, Greenberg NL, Levy ES, Yi E, Mitchell WG, Rice WJ, Wigge C, Pilli J,
1022 George EW, Aslanoglou D, Courel M, Freyberg RJ, Javitch JA, Wills ZP, Area-Gomez
1023 E, Shiva S, Bartolini F, Volchuk A, Murray SA, Aridor M, Fish KN, Walter P, Balla T,
1024 Fass D, Wolf SG, Watkins SC, Carazo JM, Jensen GJ, Frank J, Freyberg Z. 2020.
1025 Ribosome-associated vesicles: A dynamic subcompartment of the endoplasmic
1026 reticulum in secretory cells. *Sci Adv* **6**:eaay9572. doi:10.1126/sciadv.aay9572
1027 Chino H, Mizushima N. 2020. ER-Phagy: Quality Control and Turnover of Endoplasmic
1028 Reticulum. *Trends in Cell Biology* **30**:384–398. doi:10.1016/j.tcb.2020.02.001
1029 Chouhan AK, Zhang J, Zinsmaier KE, Macleod GT. 2010. Presynaptic Mitochondria in
1030 Functionally Different Motor Neurons Exhibit Similar Affinities for Ca2+ But Exert Little
1031 Influence as Ca2+ Buffers at Nerve Firing Rates In Situ. *J Neurosci* **30**:1869–1881.
1032 doi:10.1523/JNEUROSCI.4701-09.2010
1033 Christianson JC, Jarosch E, Sommer T. 2023. Mechanisms of substrate processing during ER-
1034 associated protein degradation. *Nat Rev Mol Cell Biol* 1–20. doi:10.1038/s41580-023-
1035 00633-8
1036 Costantini LM, Fossati M, Francolini M, Snapp EL. 2012. Assessing the Tendency of
1037 Fluorescent Proteins to Oligomerize under Physiologic Conditions. *Traffic* **13**:643–649.
1038 doi:10.1111/j.1600-0854.2012.01336.x
1039 Crapart C, Scott ZC, Konno T, Sharma A, Bailey DM, Avezov E, Koslover EF. 2023. Luminal
1040 transport rates through intact endoplasmic reticulum limit the magnitude of localized
1041 Ca2+ signals. doi:10.1101/2023.06.23.546357

1042 Dayel MJ, Hom EFY, Verkman AS. 1999. Diffusion of Green Fluorescent Protein in the
1043 Aqueous-Phase Lumen of Endoplasmic Reticulum. *Biophysical Journal* **76**:2843–2851.
1044 doi:10.1016/S0006-3495(99)77438-2
1045 de Juan-Sanz J, Holt GT, Schreiter ER, de Juan F, Kim DS, Ryan TA. 2017. Axonal
1046 Endoplasmic Reticulum Ca2+ Content Controls Release Probability in CNS Nerve
1047 Terminals. *Neuron* **93**:867-881.e6. doi:10.1016/j.neuron.2017.01.010
1048 Del Signore SJ, Mitzner MG, Silveira AM, Fai TG, Rodal AA. 2022. An approach for
1049 quantitative mapping of synaptic periactive zone architecture and organization. *Mol Biol*
1050 *Cell* mbcE22080372. doi:10.1091/mbc.E22-08-0372
1051 Deng C, Moradi M, Reinhard S, Ji C, Jablonka S, Hennlein L, Lüningschrör P, Doose S, Sauer
1052 M, Sendtner M. 2021. Dynamic remodeling of ribosomes and endoplasmic reticulum in
1053 axon terminals of motoneurons. *Journal of Cell Science* **134**:jcs258785.
1054 doi:10.1242/jcs.258785
1055 Deshpande M, Feiger Z, Shilton AK, Luo CC, Silverman E, Rodal AA. 2016. Role of BMP
1056 receptor traffic in synaptic growth defects in an ALS model. *MBoC* **27**:2898–2910.
1057 doi:10.1091/mbc.E16-07-0519
1058 Espadas J, Pendin D, Bocanegra R, Escalada A, Misticoni G, Trevisan T, Velasco del Olmo A,
1059 Montagna A, Bova S, Ibarra B, Kuzmin PI, Bashkirov PV, Shnyrova AV, Frolov VA,
1060 Daga A. 2019. Dynamic constriction and fission of endoplasmic reticulum membranes
1061 by reticulon. *Nat Commun* **10**:5327. doi:10.1038/s41467-019-13327-7
1062 Feng Y, Ueda A, Wu C-F. 2004. A modified minimal hemolymph-like solution, HL3.1, for
1063 physiological recordings at the neuromuscular junctions of normal and mutant
1064 Drosophila larvae. *J Neurogenet* **18**:377–402. doi:10.1080/01677060490894522
1065 Fernandes AR, Martins JP, Gomes ER, Mendes CS, Teodoro RO. 2023. Drosophila motor
1066 neuron boutons remodel through membrane blebbing coupled with muscle contraction.
1067 *Nat Commun* **14**:3352. doi:10.1038/s41467-023-38421-9
1068 Finsterer J, Löscher W, Quasthoff S, Wanschitz J, Auer-Grumbach M, Stevanin G. 2012.
1069 Hereditary spastic paraplegias with autosomal dominant, recessive, X-linked, or
1070 maternal trait of inheritance. *Journal of the Neurological Sciences* **318**:1–18.
1071 doi:10.1016/j.jns.2012.03.025
1072 Fowler PC, Garcia-Pardo ME, Simpson JC, O'Sullivan NC. 2019. NeurodegenERation: The
1073 Central Role for ER Contacts in Neuronal Function and Axonopathy, Lessons From
1074 Hereditary Spastic Paraplegias and Related Diseases. *Front Neurosci* **13**.
1075 doi:10.3389/fnins.2019.01051
1076 Friedman JR, Lackner LL, West M, DiBenedetto JR, Nunnari J, Voeltz GK. 2011. ER tubules
1077 mark sites of mitochondrial division. *Science* **334**:358–362.
1078 doi:10.1126/science.1207385
1079 Glock C, Biever A, Tushev G, Nassim-Assir B, Kao A, Bartnik I, tom Dieck S, Schuman EM.
1080 2021. The translatome of neuronal cell bodies, dendrites, and axons. *Proceedings of*
1081 *the National Academy of Sciences* **118**:e2113929118. doi:10.1073/pnas.2113929118
1082 Graf ER, Heerssen HM, Wright CM, Davis GW, DiAntonio A. 2011. Stathmin is Required for
1083 Stability of the Drosophila Neuromuscular Junction. *J Neurosci* **31**:15026–15034.
1084 doi:10.1523/JNEUROSCI.2024-11.2011
1085 Gregorio CD, Delgado R, Ibacache A, Sierralta J, Couve A. 2017. Drosophila Atlastin in motor
1086 neurons is required for locomotion and presynaptic function. *J Cell Sci* **130**:3507–3516.
1087 doi:10.1242/jcs.201657
1088 Harmansa S, Alborelli I, Bieli D, Caussinus E, Affolter M. 2017. A nanobody-based toolset to
1089 investigate the role of protein localization and dispersal in Drosophila. *eLife* **6**:e22549.
1090 doi:10.7554/eLife.22549

1091 Holcman D, Parutto P, Chambers JE, Fantham M, Young LJ, Marciniak SJ, Kaminski CF, Ron
1092 D, Avezov E. 2018. Single particle trajectories reveal active endoplasmic reticulum
1093 luminal flow. *Nat Cell Biol* **20**:1118–1125. doi:10.1038/s41556-018-0192-2
1094 Hoyer MJ, Chitwood PJ, Ebmeier CC, Striepen JF, Qi RZ, Old WM, Voeltz GK. 2018. A Novel
1095 Class of ER Membrane Proteins Regulates ER-Associated Endosome Fission. *Cell*
1096 **175**:254-265.e14. doi:10.1016/j.cell.2018.08.030
1097 Hu J, Shibata Y, Zhu P-P, Voss C, Rismanchi N, Prinz WA, Rapoport TA, Blackstone C. 2009.
1098 A Class of Dynamin-like GTPases Involved in the Generation of the Tubular ER
1099 Network. *Cell* **138**:549–561. doi:10.1016/j.cell.2009.05.025
1100 Hu X, Wu F, Sun S, Yu W, Hu J. 2015. Human atlastin GTPases mediate differentiated fusion
1101 of endoplasmic reticulum membranes. *Protein Cell* **6**:307–311. doi:10.1007/s13238-
1102 015-0139-3
1103 Igbaria A, Merksamer PI, Trusina A, Tilahun F, Johnson JR, Brandman O, Krogan NJ,
1104 Weissman JS, Papa FR. 2019. Chaperone-mediated reflux of secretory proteins to the
1105 cytosol during endoplasmic reticulum stress. *Proc Natl Acad Sci U S A* **116**:11291–
1106 11298. doi:10.1073/pnas.1904516116
1107 King C, Sengupta P, Seo AY, Lippincott-Schwartz J. 2020. ER membranes exhibit phase
1108 behavior at sites of organelle contact. *Proceedings of the National Academy of*
1109 *Sciences* **117**:7225–7235. doi:10.1073/pnas.1910854117
1110 Lai Y-S, Stefano G, Brandizzi F. 2014. ER stress signaling requires RHD3, a functionally
1111 conserved ER-shaping GTPase. *Journal of Cell Science* **127**:3227–3232.
1112 doi:10.1242/jcs.147447
1113 Lajoie P, Snapp EL. 2020. Size-dependent secretory protein reflux into the cytosol in
1114 association with acute endoplasmic reticulum stress. *Traffic* **21**:419–429.
1115 doi:10.1111/tra.12729
1116 Le Gall S, Neuhof A, Rapoport T. 2004. The Endoplasmic Reticulum Membrane Is Permeable
1117 to Small Molecules. *MBoC* **15**:447–455. doi:10.1091/mbc.e03-05-0325
1118 Lee M, Paik SK, Lee M-J, Kim Y-J, Kim S, Nahm M, Oh S-J, Kim H-M, Yim J, Lee CJ, Bae YC,
1119 Lee S. 2009. Drosophila Atlastin regulates the stability of muscle microtubules and is
1120 required for synapse development. *Developmental Biology* **330**:250–262.
1121 doi:10.1016/j.ydbio.2009.03.019
1122 Lippincott-Schwartz J, Snapp EL, Phair RD. 2018. The Development and Enhancement of
1123 FRAP as a Key Tool for Investigating Protein Dynamics. *Biophys J* **115**:1146–1155.
1124 doi:10.1016/j.bpj.2018.08.007
1125 Liu X, Guo X, Niu L, Li X, Sun F, Hu J, Wang X, Shen K. 2019. Atlastin-1 regulates
1126 morphology and function of endoplasmic reticulum in dendrites. *Nat Commun* **10**:1–15.
1127 doi:10.1038/s41467-019-08478-6
1128 Lu L, Ladinsky MS, Kirchhausen T. 2009. Cisternal Organization of the Endoplasmic Reticulum
1129 during Mitosis. *MBoC* **20**:3471–3480. doi:10.1091/mbc.e09-04-0327
1130 Lü L, Niu L, Hu J. 2020. “At last in” the physiological roles of the tubular ER network. *Biophys*
1131 *Rep* **6**:105–114. doi:10.1007/s41048-020-00113-y
1132 Lu M, Tartwijk FW van, Lin JQ, Nijenhuis W, Parutto P, Fantham M, Christensen CN, Avezov
1133 E, Holt CE, Tunnacliffe A, Holcman D, Kapitein L, Schierle GSK, Kaminski CF. 2020.
1134 The structure and global distribution of the endoplasmic reticulum network are actively
1135 regulated by lysosomes. *Science Advances* **6**:eabc7209. doi:10.1126/sciadv.abc7209
1136 McKibbin C, Mares A, Piacenti M, Williams H, Roboti P, Puumalainen M, Callan AC, Lesiak-
1137 Mieczkowska K, Linder S, Harant H, High S, Flitsch SL, Whitehead RC, Swanton E.
1138 2012. Inhibition of protein translocation at the endoplasmic reticulum promotes

activation of the unfolded protein response. *Biochemical Journal* **442**:639–648. doi:10.1042/BJ20111220

Merighi A, Lossi L. 2022. Endoplasmic Reticulum Stress Signaling and Neuronal Cell Death. *International Journal of Molecular Sciences* **23**:15186. doi:10.3390/ijms232315186

Niu L, Ma T, Yang F, Yan B, Tang X, Yin H, Wu Q, Huang Y, Yao Z-P, Wang J, Guo Y, Hu J. 2019. Atlastin-mediated membrane tethering is critical for cargo mobility and exit from the endoplasmic reticulum. *PNAS* **116**:14029–14038. doi:10.1073/pnas.1908409116

Obara CJ, Nixon-Abell J, Moore AS, Riccio F, Hoffman DP, Shtengel G, Xu CS, Schaefer K, Pasolli HA, Masson J-B, Hess HF, Calderon CP, Blackstone C, Lippincott-Schwartz J. 2024. Motion of VAPB molecules reveals ER-mitochondria contact site subdomains. *Nature* **626**:169–176. doi:10.1038/s41586-023-06956-y

Oliva MK, Pérez-Moreno JJ, O'Shaughnessy J, Wardill TJ, O'Kane CJ. 2020. Endoplasmic Reticulum Lumenal Indicators in Drosophila Reveal Effects of HSP-Related Mutations on Endoplasmic Reticulum Calcium Dynamics. *Front Neurosci* **14**. doi:10.3389/fnins.2020.00816

Orso G, Pendin D, Liu S, Tosetto J, Moss TJ, Faust JE, Micaroni M, Egorova A, Martinuzzi A, McNew JA, Daga A. 2009. Homotypic fusion of ER membranes requires the dynamin-like GTPase Atlastin. *Nature* **460**:978–983. doi:10.1038/nature08280

O'Sullivan NC, Jahn TR, Reid E, O'Kane CJ. 2012. Reticulon-like-1, the Drosophila orthologue of the Hereditary Spastic Paraplegia gene reticulon 2, is required for organization of endoplasmic reticulum and of distal motor axons. *Hum Mol Genet* **21**:3356–3365. doi:10.1093/hmg/dds167

Özkan N, Koppers M, van Soest I, van Harten A, Jurriens D, Liv N, Klumperman J, Kapitein LC, Hoogenraad CC, Farías GG. 2021. ER - lysosome contacts at a pre-axonal region regulate axonal lysosome availability. *Nat Commun* **12**:4493. doi:10.1038/s41467-021-24713-5

Öztürk Z, O'Kane CJ, Pérez-Moreno JJ. 2020. Axonal Endoplasmic Reticulum Dynamics and Its Roles in Neurodegeneration. *Frontiers in Neuroscience* **14**:1–33. doi:10.3389/fnins.2020.00048

Perez-Alvarez A, Yin S, Schulze C, Hammer JA, Wagner W, Oertner TG. 2020. Endoplasmic reticulum visits highly active spines and prevents runaway potentiation of synapses. *Nature Communications* **11**:5083. doi:10.1038/s41467-020-18889-5

Pérez-Moreno JJ, Smith RC, Oliva MK, Gallo F, Ojha S, Müller KH, O'Kane CJ. 2023. Drosophila SPG12 ortholog, reticulon-like 1, governs presynaptic ER organization and Ca2+ dynamics. *J Cell Biol* **222**:e202112101. doi:10.1083/jcb.202112101

Raffaello A, Mammucari C, Gherardi G, Rizzuto R. 2016. Calcium at the Center of Cell Signaling: Interplay between Endoplasmic Reticulum, Mitochondria, and Lysosomes. *Trends in Biochemical Sciences* **41**:1035–1049. doi:10.1016/j.tibs.2016.09.001

Raiborg C, Wenzel EM, Pedersen NM, Olsvik H, Schink KO, Schultz SW, Vietri M, Nisi V, Bucci C, Brech A, Johansen T, Stenmark H. 2015. Repeated ER–endosome contacts promote endosome translocation and neurite outgrowth. *Nature* **520**:234–238. doi:10.1038/nature14359

Rao K, Stone MC, Weiner AT, Gheres KW, Zhou C, Deitcher DL, Levitan ES, Rolls MM. 2016. Spastin, atlastin, and ER relocalization are involved in axon but not dendrite regeneration. *MBoC* **27**:3245–3256. doi:10.1091/mbc.E16-05-0287

Read A, Schröder M. 2021. The Unfolded Protein Response: An Overview. *Biology (Basel)* **10**:384. doi:10.3390/biology10050384

1186 Rismanchi N, Soderblom C, Stadler J, Zhu P-P, Blackstone C. 2008. Atlastin GTPases are
1187 required for Golgi apparatus and ER morphogenesis. *Hum Mol Genet* **17**:1591–1604.
1188 doi:10.1093/hmg/ddn046
1189 Roos J, Hummel T, Ng N, Klämbt C, Davis GW. 2000. *Drosophila* Futsch Regulates Synaptic
1190 Microtubule Organization and Is Necessary for Synaptic Growth. *Neuron* **26**:371–382.
1191 doi:10.1016/S0896-6273(00)81170-8
1192 Rowland AA, Chitwood PJ, Phillips MJ, Voeltz GK. 2014. ER Contact Sites Define the Position
1193 and Timing of Endosome Fission. *Cell* **159**:1027–1041. doi:10.1016/j.cell.2014.10.023
1194 Schwarz DS, Blower MD. 2016. The endoplasmic reticulum: structure, function and response
1195 to cellular signaling. *Cell Mol Life Sci* **73**:79–94. doi:10.1007/s00018-015-2052-6
1196 Scott ZC, Brown AI, Mogre SS, Westrate LM, Koslover EF. 2021. Diffusive search and
1197 trajectories on tubular networks: a propagator approach. *Eur Phys J E* **44**:80.
1198 doi:10.1140/epje/s10189-021-00083-0
1199 Shibata Y, Mazur EE, Pan B, Paulo JA, Gygi SP, Chavan S, Valerio LSA, Zhang J, Rapoport
1200 TA. 2024. The membrane curvature-inducing REEP1-4 proteins generate an ER-
1201 derived vesicular compartment. *Nat Commun* **15**:8655. doi:10.1038/s41467-024-52901-
1202 6
1203 Sicari D, Centonze FG, Pineau R, Le Reste P-J, Negroni L, Chat S, Mohtar MA, Thomas D,
1204 Gillet R, Hupp T, Chevet E, Igbaria A. 2021. Reflux of Endoplasmic Reticulum proteins
1205 to the cytosol inactivates tumor suppressors. *EMBO Rep* **22**:e51412.
1206 doi:10.15252/embr.202051412
1207 Snow PM, Patel NH, Harrelson AL, Goodman CS. 1987. Neural-specific carbohydrate moiety
1208 shared by many surface glycoproteins in Drosophila and grasshopper embryos. *J*
1209 *Neurosci* **7**:4137–4144. doi:10.1523/JNEUROSCI.07-12-04137.1987
1210 Spits M, Neefjes J. 2021. Mobile late endosomes modulate peripheral endoplasmic reticulum
1211 network architecture. *EMBO reports* **22**:e50815. doi:10.15252/embr.202050815
1212 Subramanian K, Meyer T. 1997. Calcium-Induced Restructuring of Nuclear Envelope and
1213 Endoplasmic Reticulum Calcium Stores. *Cell* **89**:963–971. doi:10.1016/S0092-
1214 8674(00)80281-0
1215 Summerville JB, Faust JF, Fan E, Pendin D, Daga A, Formella J, Stern M, McNew JA. 2016.
1216 The effects of ER morphology on synaptic structure and function in Drosophila
1217 melanogaster. *J Cell Sci* **129**:1635–1648. doi:10.1242/jcs.184929
1218 Sun L, Yu F, Ullah A, Hubrack S, Daalis A, Jung P, Machaca K. 2011. Endoplasmic Reticulum
1219 Remodeling Tunes IP3-Dependent Ca2+ Release Sensitivity. *PLOS ONE* **6**:e27928.
1220 doi:10.1371/journal.pone.0027928
1221 Thevenaz P, Ruttimann UE, Unser M. 1998. A pyramid approach to subpixel registration
1222 based on intensity. *IEEE Trans on Image Process* **7**:27–41. doi:10.1109/83.650848
1223 Wang S, Tukachinsky H, Romano FB, Rapoport TA. 2016. Cooperation of the ER-shaping
1224 proteins atlastin, lunapark, and reticulons to generate a tubular membrane network.
1225 *eLife* **5**:e18605. doi:10.7554/eLife.18605
1226 Wang X, Olberding KE, White C, Li C. 2011. Bcl-2 proteins regulate ER membrane
1227 permeability to luminal proteins during ER stress-induced apoptosis. *Cell Death Differ*
1228 **18**:38–47. doi:10.1038/cdd.2010.68
1229 Wu X, Rapoport TA. 2018. Mechanistic insights into ER-associated protein degradation. *Curr*
1230 *Opin Cell Biol* **53**:22–28. doi:10.1016/j.ceb.2018.04.004
1231 Wu Y, Whiteus C, Xu CS, Hayworth KJ, Weinberg RJ, Hess HF, Camilli PD. 2017. Contacts
1232 between the endoplasmic reticulum and other membranes in neurons. *PNAS*
1233 **114**:E4859–E4867. doi:10.1073/pnas.1701078114

1234 Yalçın B, Zhao L, Stofanko M, O'Sullivan NC, Kang ZH, Roost A, Thomas MR, Zaessinger S,
1235 Blard O, Patto AL, Sohail A, Baena V, Terasaki M, O'Kane CJ. 2017. Modeling of
1236 axonal endoplasmic reticulum network by spastic paraplegia proteins. *eLife* **6**:1–27.
1237 doi:10.7554/eLife.23882
1238 Zamponi E, Meehl JB, Voeltz GK. 2022. The ER ladder is a unique morphological feature of
1239 developing mammalian axons. *Dev Cell* **57**:1369-1382.e6.
1240 doi:10.1016/j.devcel.2022.05.002
1241 Zhao G, Zhu P-P, Renvoisé B, Maldonado-Báez L, Park SH, Blackstone C. 2016. Mammalian
1242 knock out cells reveal prominent roles for atlastin GTPases in ER network morphology.
1243 *Experimental Cell Research* **349**:32–44. doi:10.1016/j.yexcr.2016.09.015
1244 Zhu P-P, Hung H-F, Batchenkova N, Nixon-Abell J, Henderson J, Zheng P, Renvoisé B, Pang
1245 S, Xu CS, Saalfeld S, Funke J, Xie Y, Svara F, Hess HF, Blackstone C. 2022.
1246 Transverse endoplasmic reticulum expansion in hereditary spastic paraplegia
1247 corticospinal axons. *Hum Mol Genet* **31**:2779–2795. doi:10.1093/hmg/ddac072
1248 Zhu P-P, Soderblom C, Tao-Cheng J-H, Stadler J, Blackstone C. 2006. SPG3A protein
1249 atlastin-1 is enriched in growth cones and promotes axon elongation during neuronal
1250 development. *Hum Mol Genet* **15**:1343–1353. doi:10.1093/hmg/ddl054
1251
1252
1253

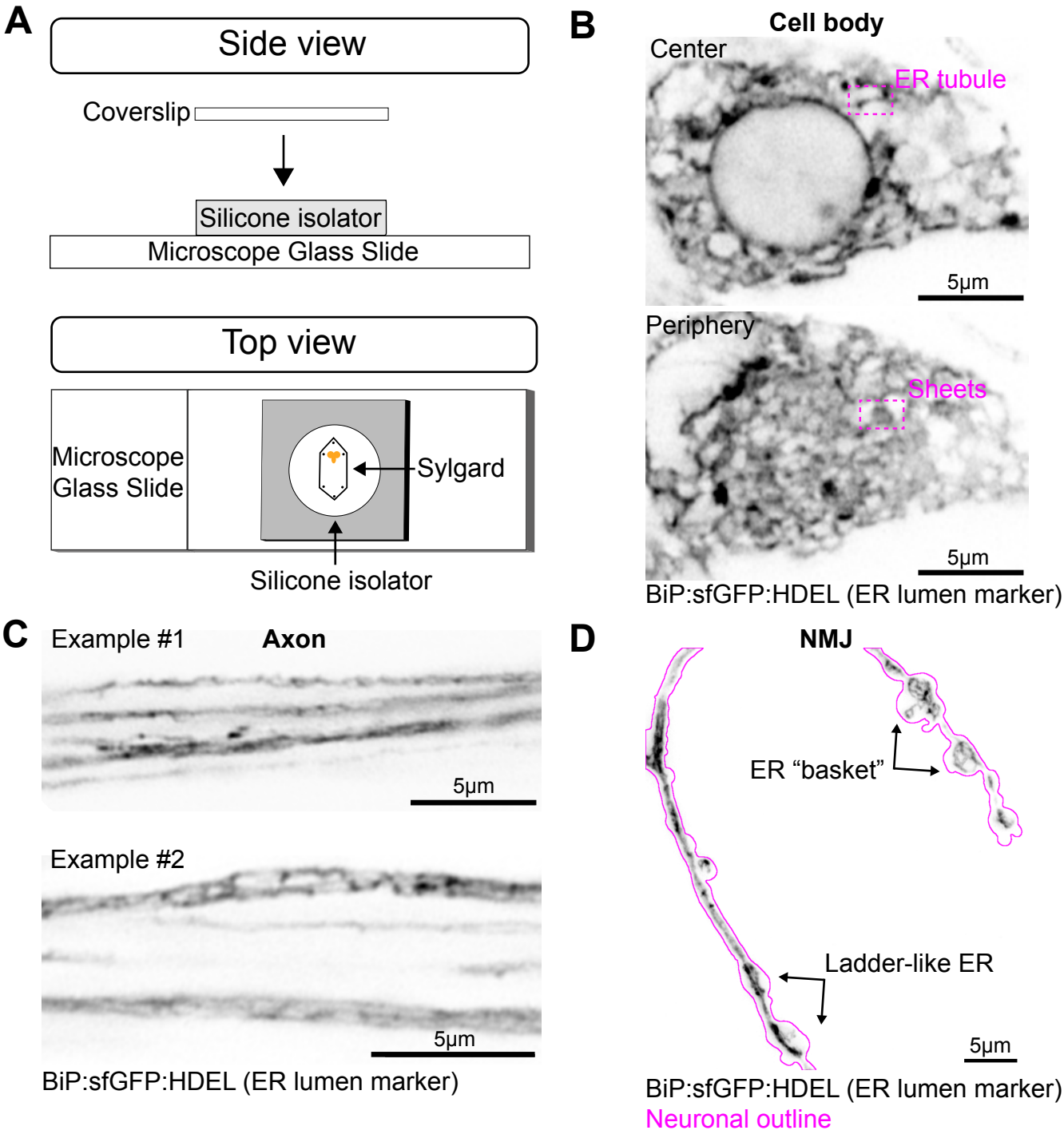
A
Side view
Coverslip
Silicone isolator
Microscope Glass Slide
Top view
Microscope Glass Slide
Sylgard
Silicone isolator
B
Cell body
Center
ER tubule
5µm
Periphery
Sheets
5µm
BiP:sfGFP:HDEL (ER lumen marker)
C
Example #1
Axon
5µm
Example #2
5µm
BiP:sfGFP:HDEL (ER lumen marker)
D
NMJ
ER "basket"
Ladder-like ER
5µm
BiP:sfGFP:HDEL (ER lumen marker)
Neuronal outline

Figure 1

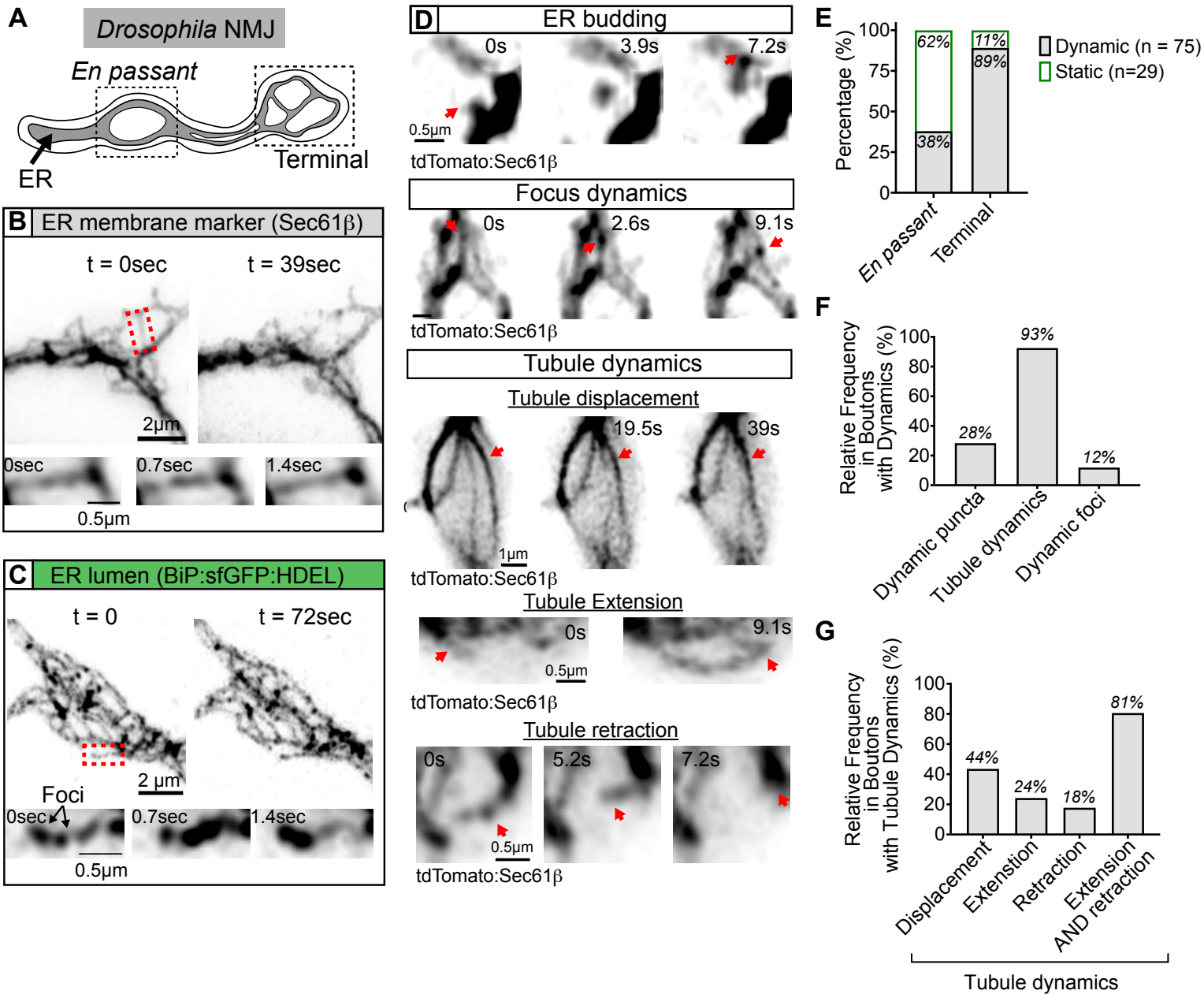
A
Drosophila NMJ
En passant
ER
Terminal
B
ER membrane marker (Sec61β)
t = 0sec
t = 39sec
2μm
0sec
0.7sec
1.4sec
0.5μm
C
ER lumen (BiP:sfGFP:HDEL)
t = 0
t = 72sec
2 μm
Foci
0sec
0.7sec
1.4sec
0.5μm
D
ER budding
0s
3.9s
7.2s
0.5μm
tdTomato:Sec61β
Focus dynamics
0s
2.6s
9.1s
tdTomato:Sec61β
Tubule dynamics
Tubule displacement
19.5s
39s
1μm
tdTomato:Sec61β
Tubule Extension
0s
9.1s
0.5μm
tdTomato:Sec61β
Tubule retraction
0s
5.2s
7.2s
0.5μm
tdTomato:Sec61β
E
Percentage (%)
100
75
50
25
0
62%
38%
11%
89%
Dynamic (n = 75)
Static (n=29)
En passant
Terminal
F
Relative Frequency in Boutons with Dynamics (%)
100
80
60
40
20
0
28%
93%
12%
Dynamic puncta
Tubule dynamics
Dynamic foci
G
Relative Frequency in Boutons with Tubule Dynamics (%)
100
80
60
40
20
0
44%
24%
18%
81%
Displacement
Extension
Retraction
Extension AND retraction
Tubule dynamics

Figure 2

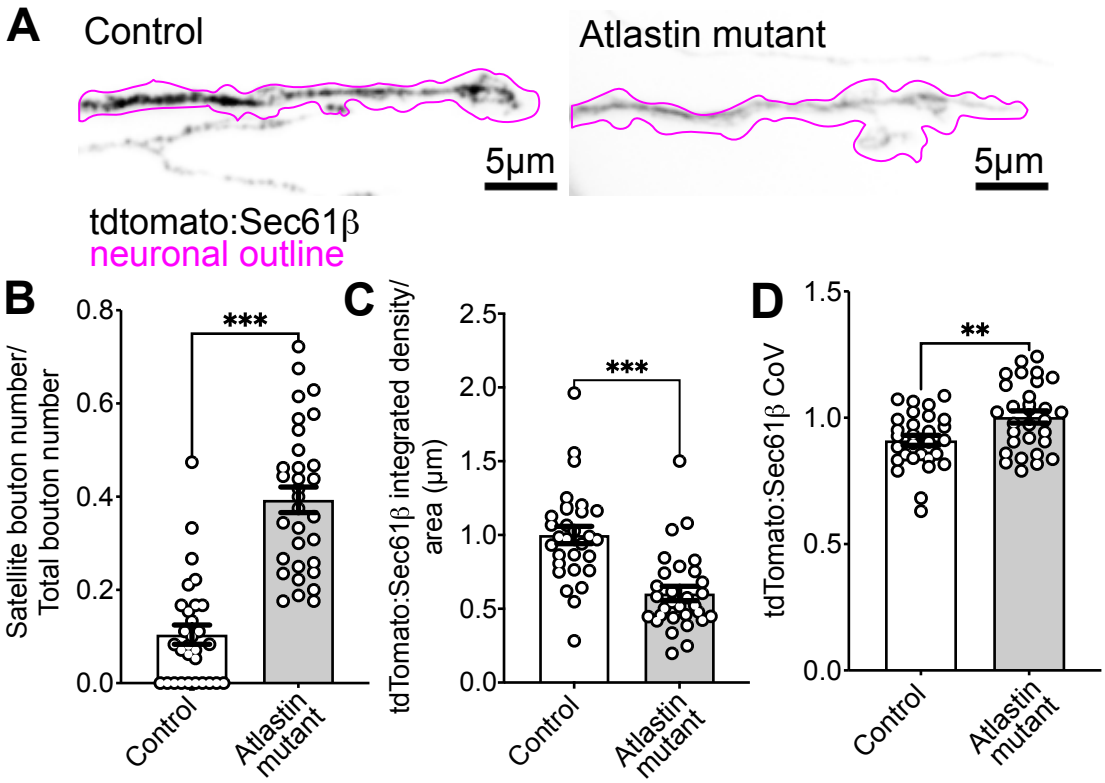
A
Control
Atlastin mutant
5μm
5μm
tdtomato:Sec61β
neuronal outline
B
Satellite bouton number/
Total bouton number
0.8
0.6
0.4
0.2
0.0
***
Control
Atlastin mutant
C
tdTomato:Sec61β integrated density/
area (μm)
2.5
2.0
1.5
1.0
0.5
0.0
***
Control
Atlastin mutant
D
tdTomato:Sec61β CoV
1.5
1.0
0.5
0.0
**
Control
Atlastin mutant

Figure 3

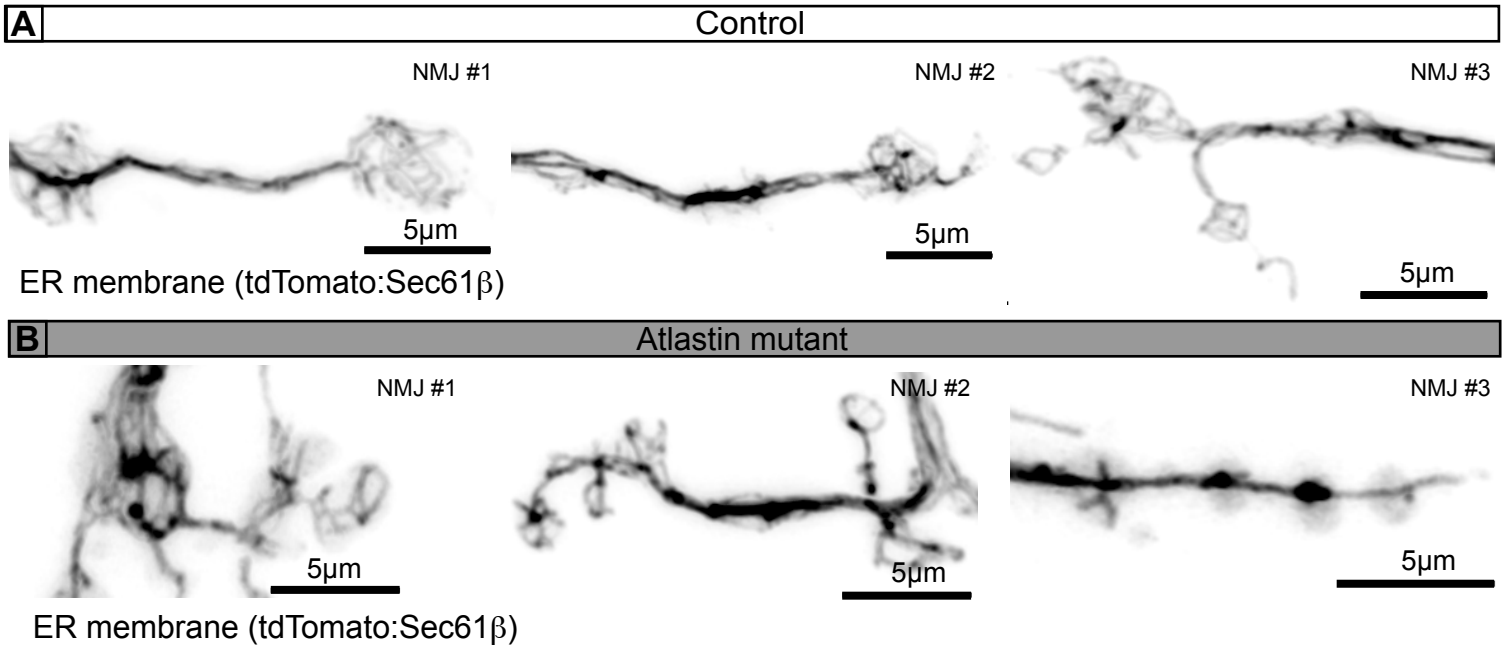

Figure 3- Supplement

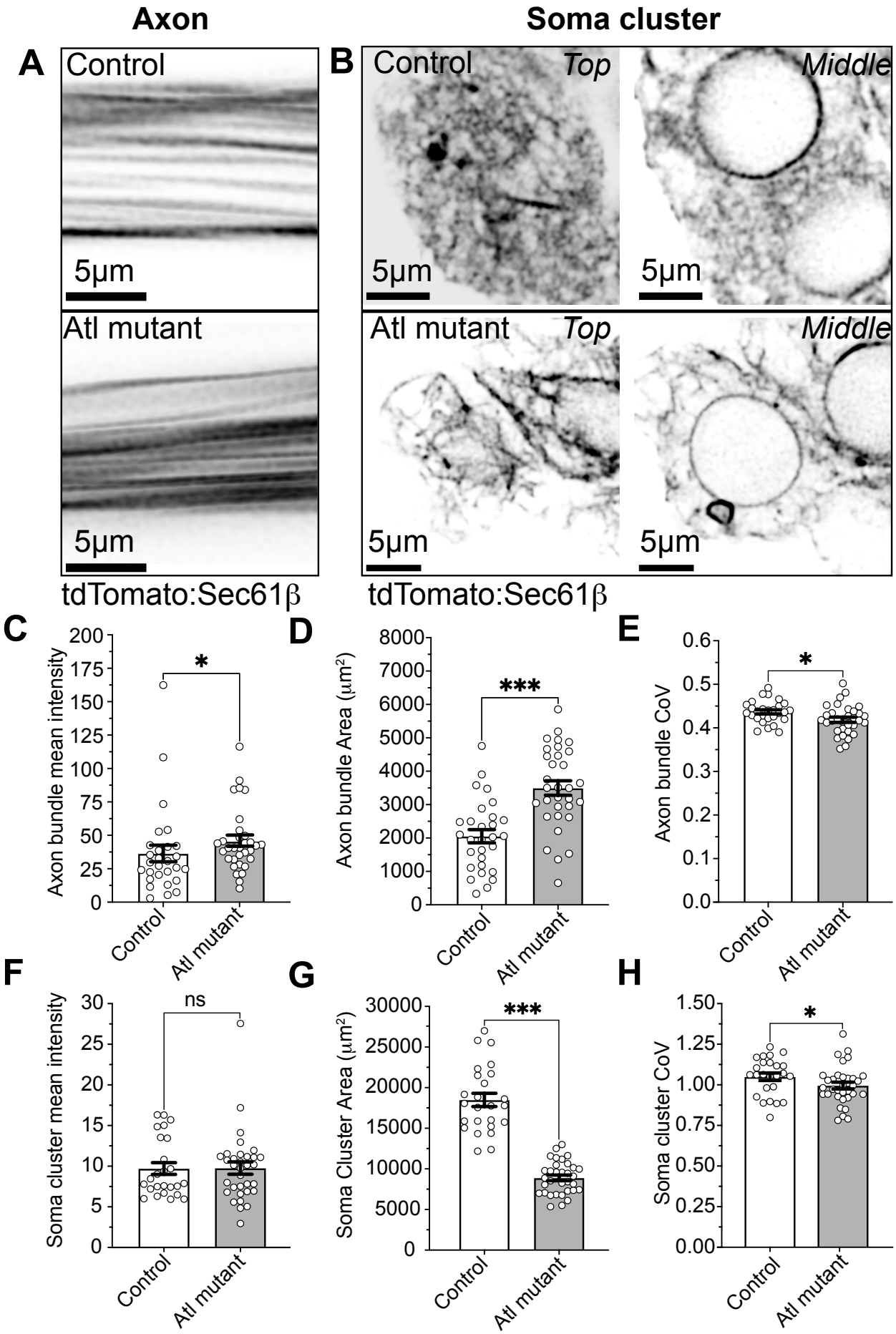
Axon
Soma cluster
A
Control
5µm
Atl mutant
5µm
B
Control
Top
Middle
5µm
5µm
Atl mutant
Top
Middle
5µm
5µm
tdTomato:Sec61β
tdTomato:Sec61β
C
Axon bundle mean intensity
*
Control
Atl mutant
D
Axon bundle Area (µm²)
***
Control
Atl mutant
E
Axon bundle CoV
*
Control
Atl mutant
F
Soma cluster mean intensity
ns
Control
Atl mutant
G
Soma Cluster Area (µm²)
***
Control
Atl mutant
H
Soma cluster CoV
*
Control
Atl mutant

Figure 4

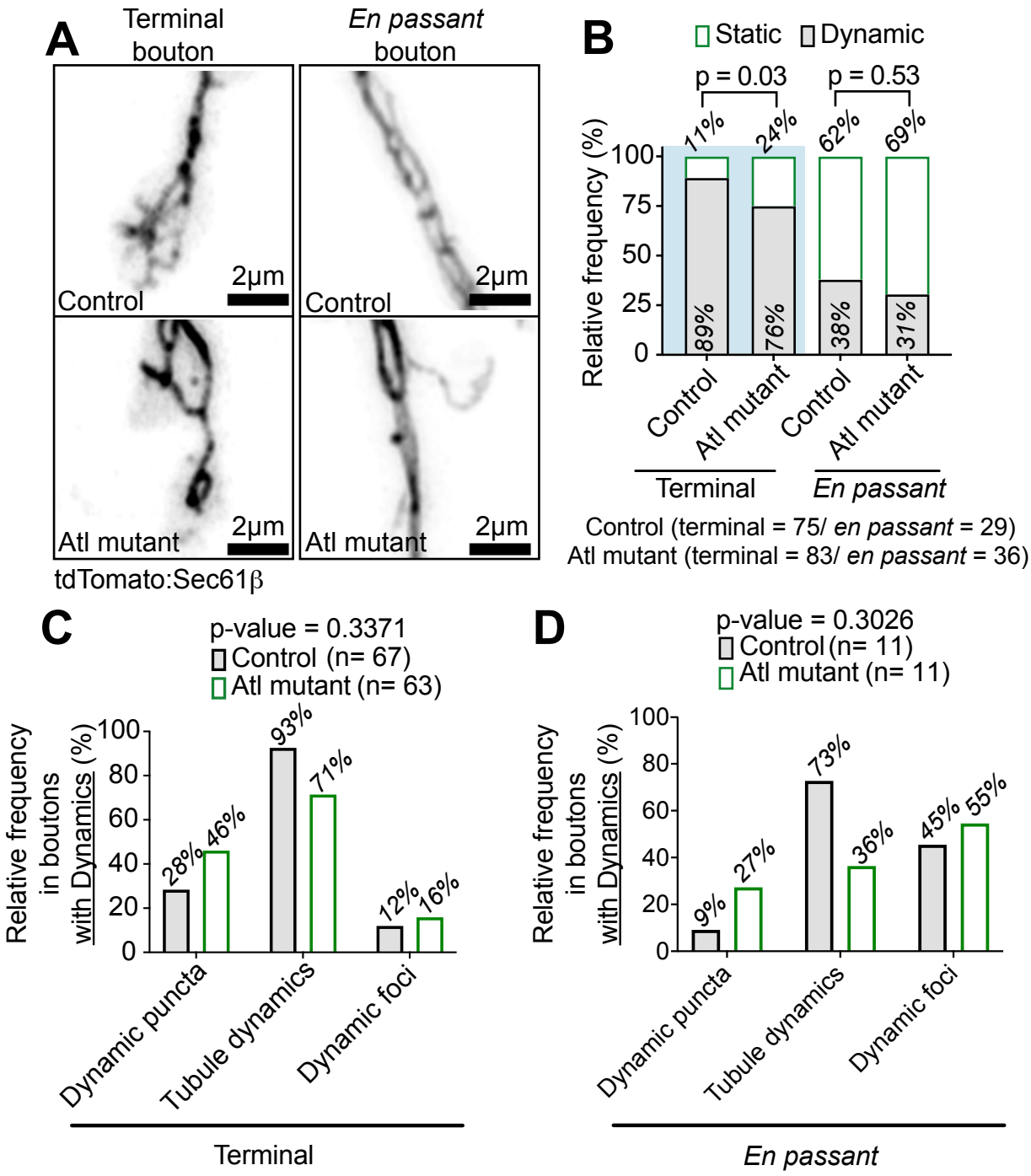
A
Terminal bouton
En passant bouton
Control
Control
Atl mutant
Atl mutant
2µm
tdTomato:Sec61β
B
Static
Dynamic
p = 0.03
p = 0.53
Relative frequency (%)
11%
24%
62%
69%
89%
76%
38%
31%
Control
Atl mutant
Control
Atl mutant
Terminal
En passant
Control (terminal = 75/ en passant = 29)
Atl mutant (terminal = 83/ en passant = 36)
C
p-value = 0.3371
Control (n= 67)
Atl mutant (n= 63)
Relative frequency in boutons with Dynamics (%)
28%
46%
93%
71%
12%
16%
Dynamic puncta
Tubule dynamics
Dynamic foci
Terminal
D
p-value = 0.3026
Control (n= 11)
Atl mutant (n= 11)
Relative frequency in boutons with Dynamics (%)
9%
27%
73%
36%
45%
55%
Dynamic puncta
Tubule dynamics
Dynamic foci
En passant

Figure 5

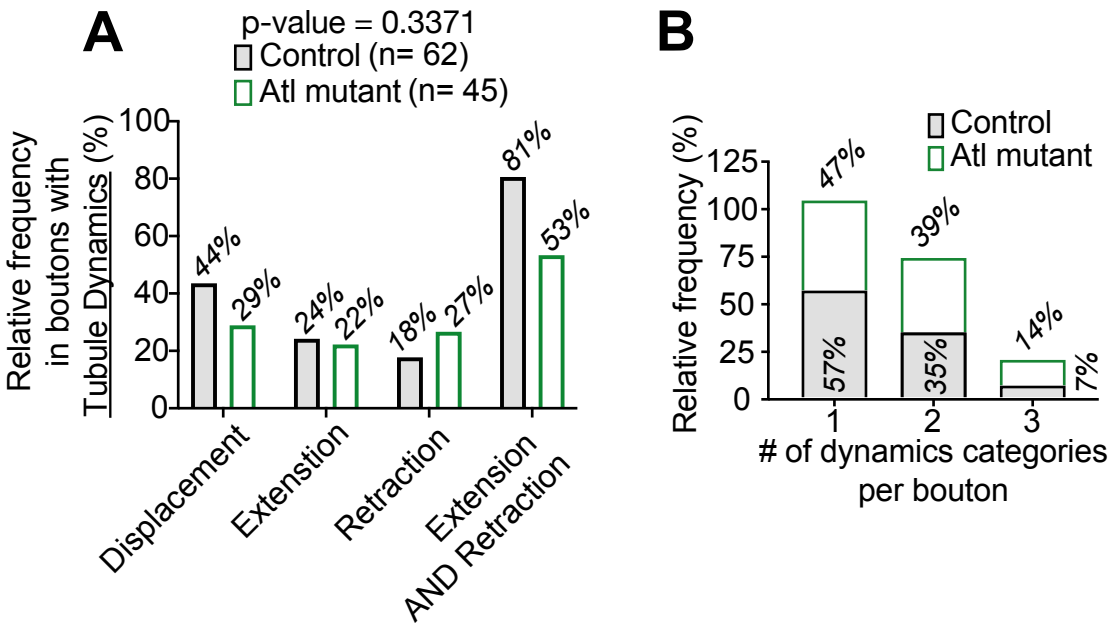

Figure 5-Supplement

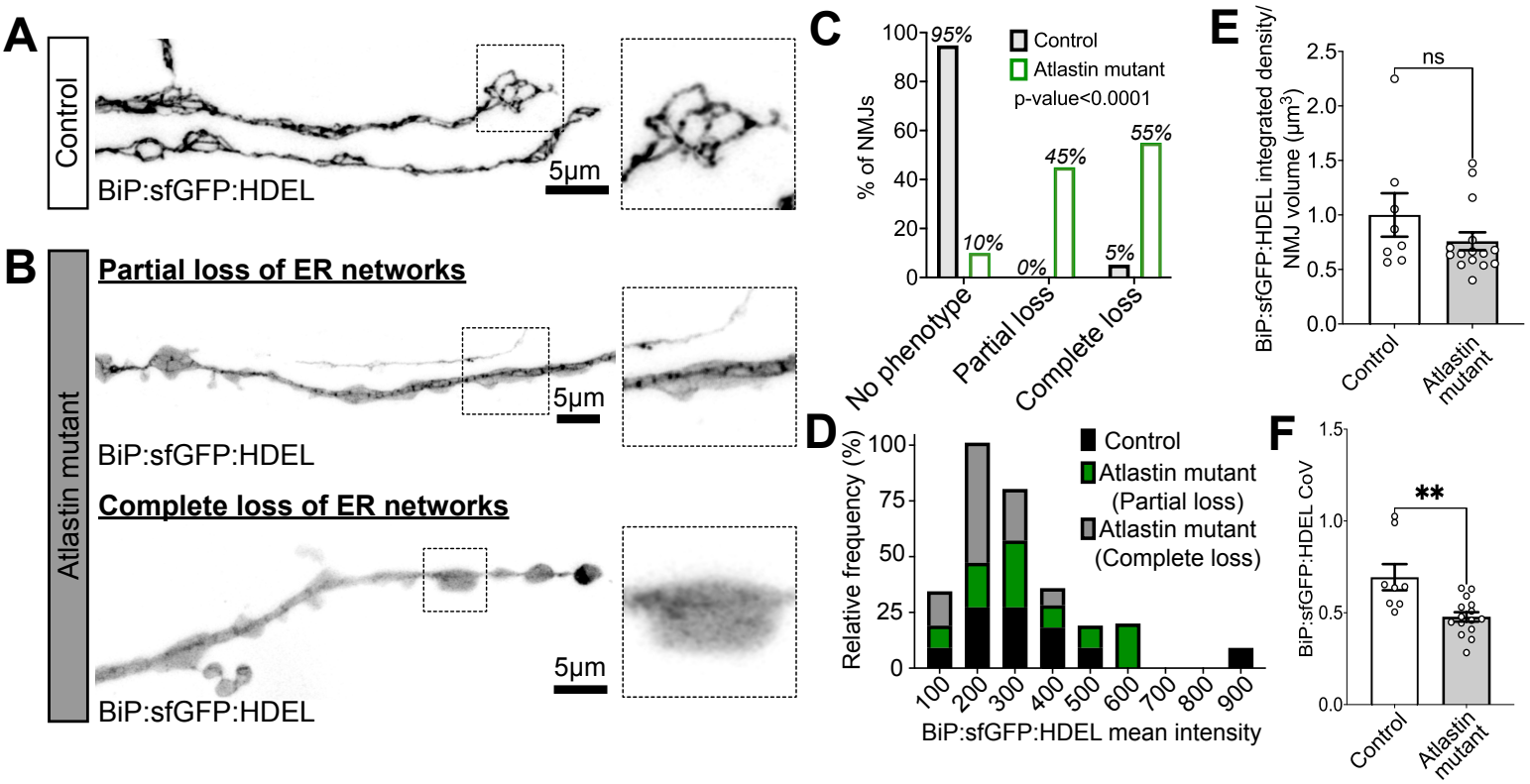
A
Control
BiP:sfGFP:HDEL
5µm
B
Atlastin mutant
Partial loss of ER networks
BiP:sfGFP:HDEL
5µm
Complete loss of ER networks
BiP:sfGFP:HDEL
5µm
C
% of NMJs
Control
Atlastin mutant
p-value<0.0001
95%
10%
0%
45%
5%
55%
No phenotype
Partial loss
Complete loss
D
Relative frequency (%)
Control
Atlastin mutant (Partial loss)
Atlastin mutant (Complete loss)
BiP:sfGFP:HDEL mean intensity
E
BiP:sfGFP:HDEL integrated density/ NMJ volume (µm³)
ns
Control
Atlastin mutant
F
BiP:sfGFP:HDEL CoV
**
Control
Atlastin mutant

Figure 6

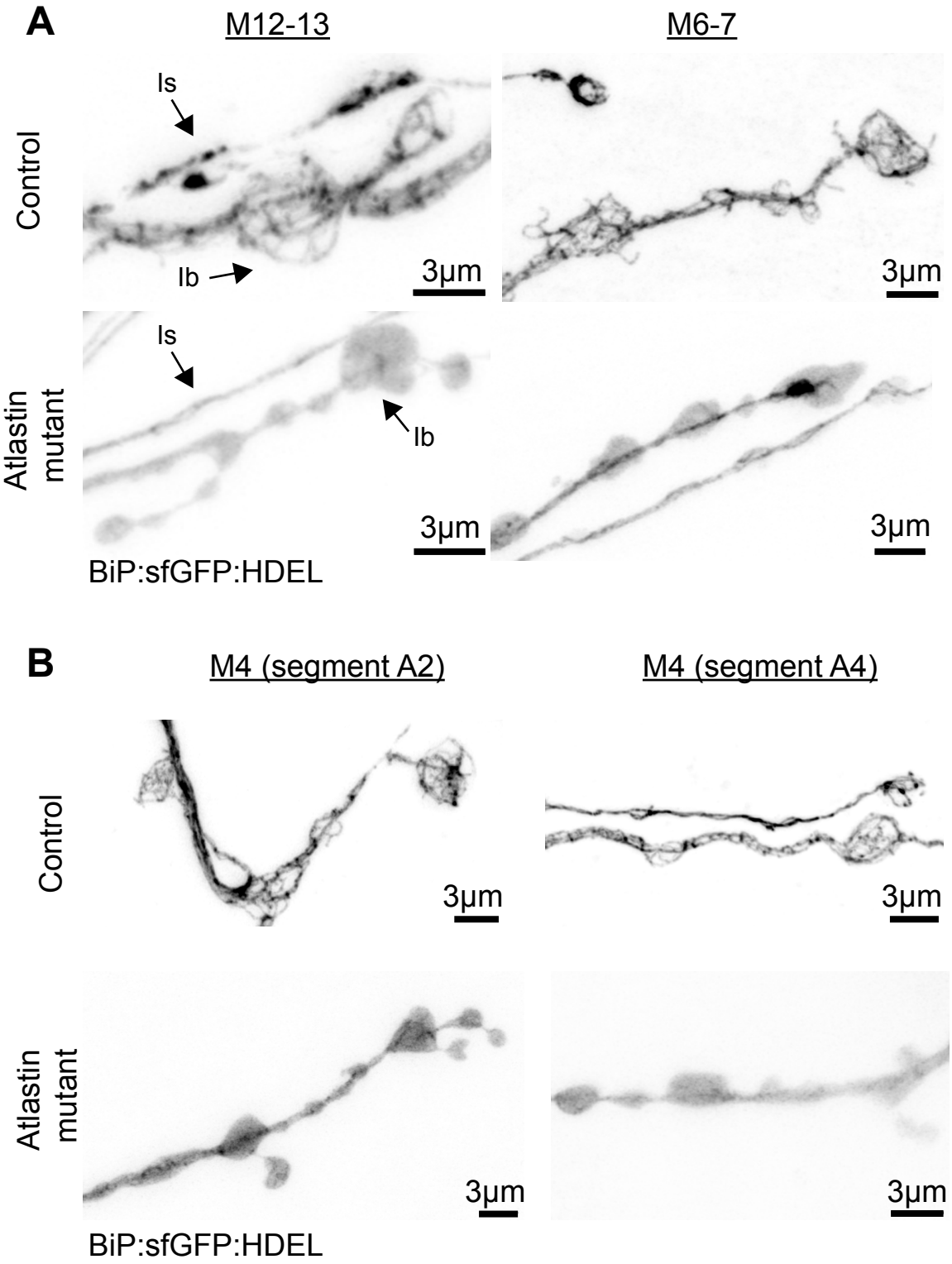

Figure 6- Supplement

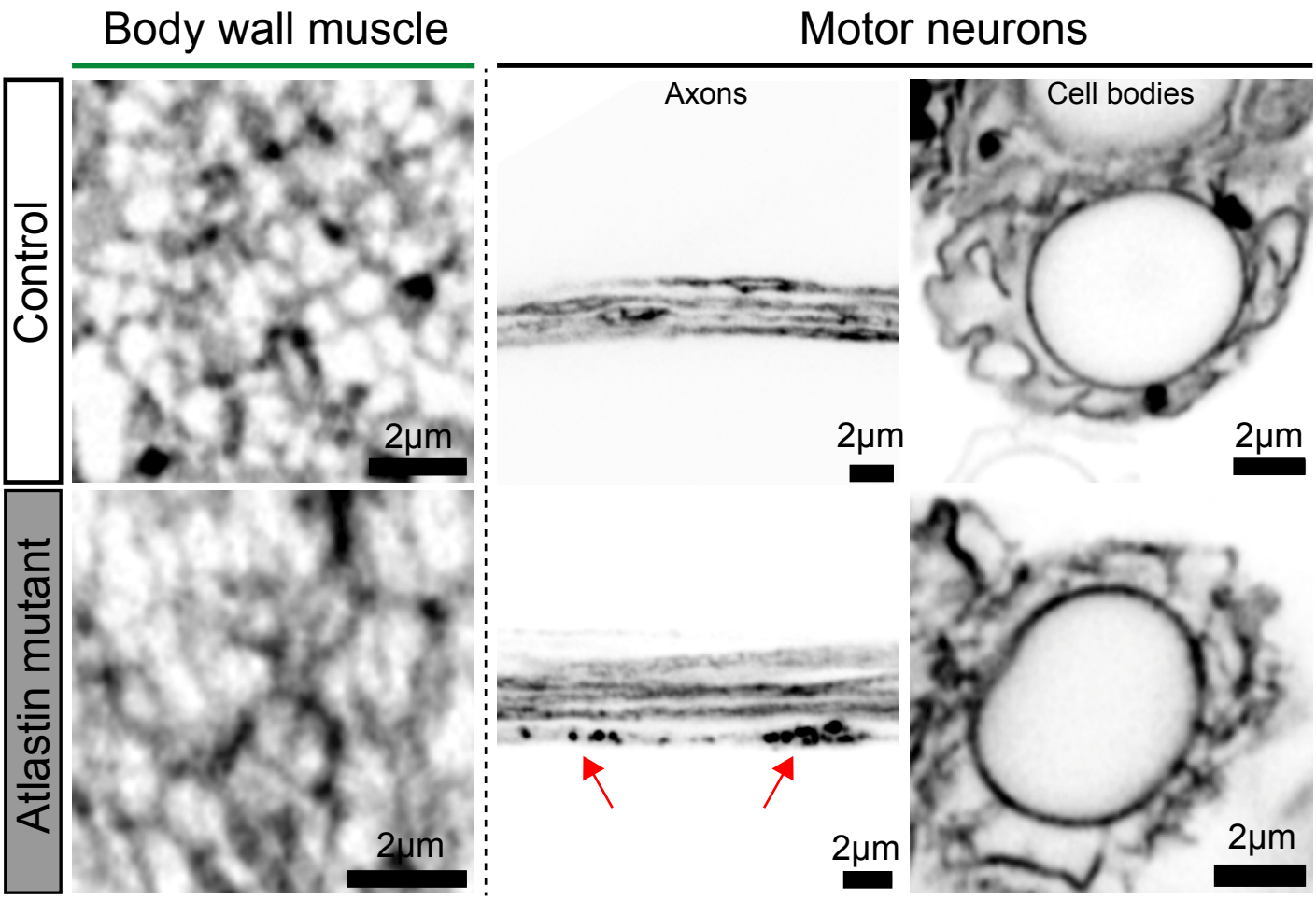
Body wall muscle
Motor neurons
Axons
Cell bodies
Control
Atlastin mutant
2µm
2µm
2µm
2µm
2µm
2µm

Figure 7

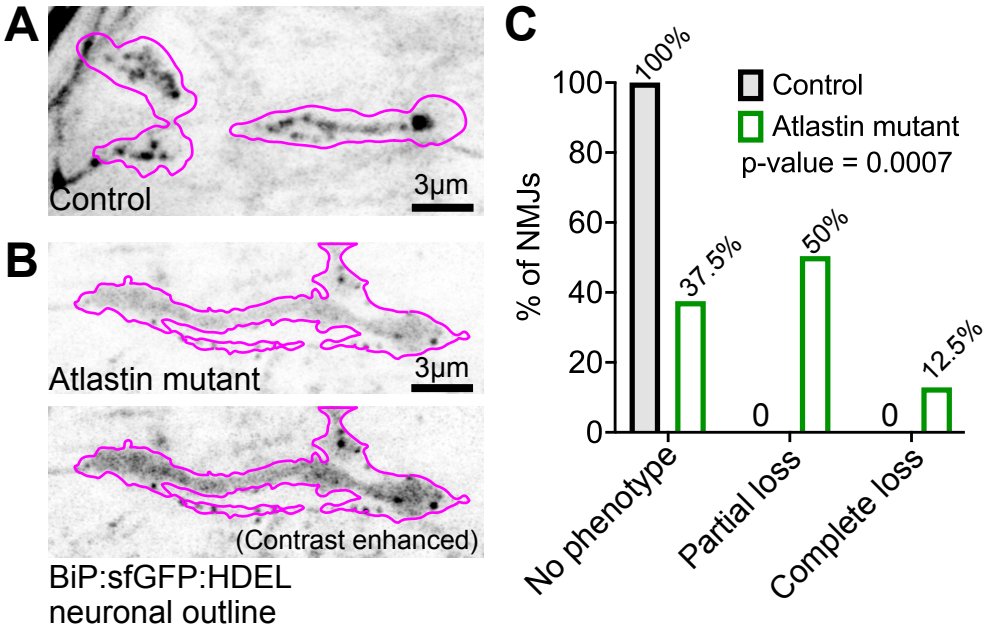
A
Control
3μm
B
Atlastin mutant
3μm
(Contrast enhanced)
BiP:sfGFP:HDEL
neuronal outline
C
Control
Atlastin mutant
p-value = 0.0007
% of NMJs
100
80
60
40
20
0
100%
37.5%
0
50%
0
12.5%
No phenotype
Partial loss
Complete loss

Figure 8

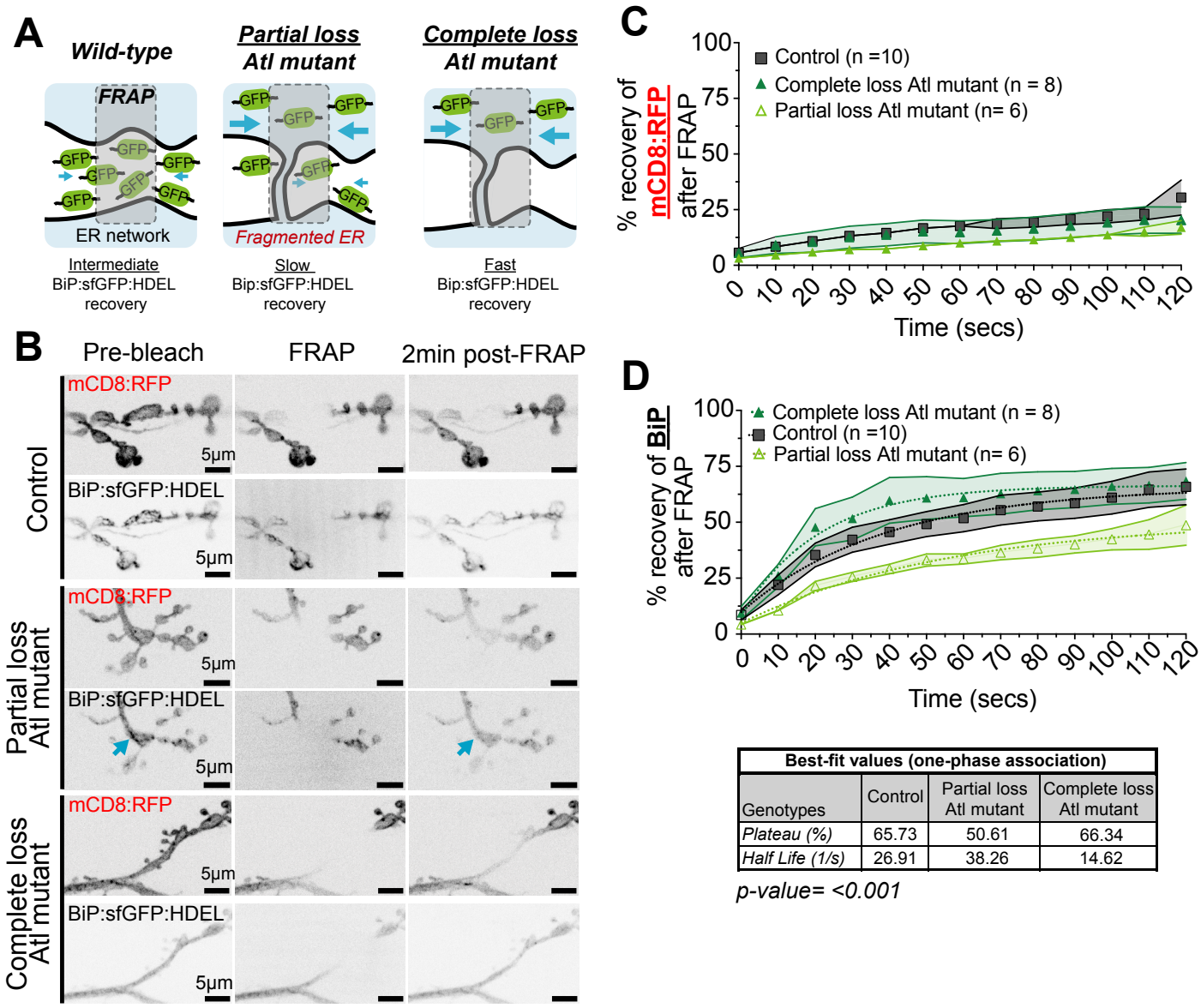

Best-fit values (one-phase association)			
Genotypes	Control	Partial loss Atl mutant	Complete loss Atl mutant
Plateau (%)	65.73	50.61	66.34
Half Life (1/s)	26.91	38.26	14.62

p-value= <0.001

Figure 9

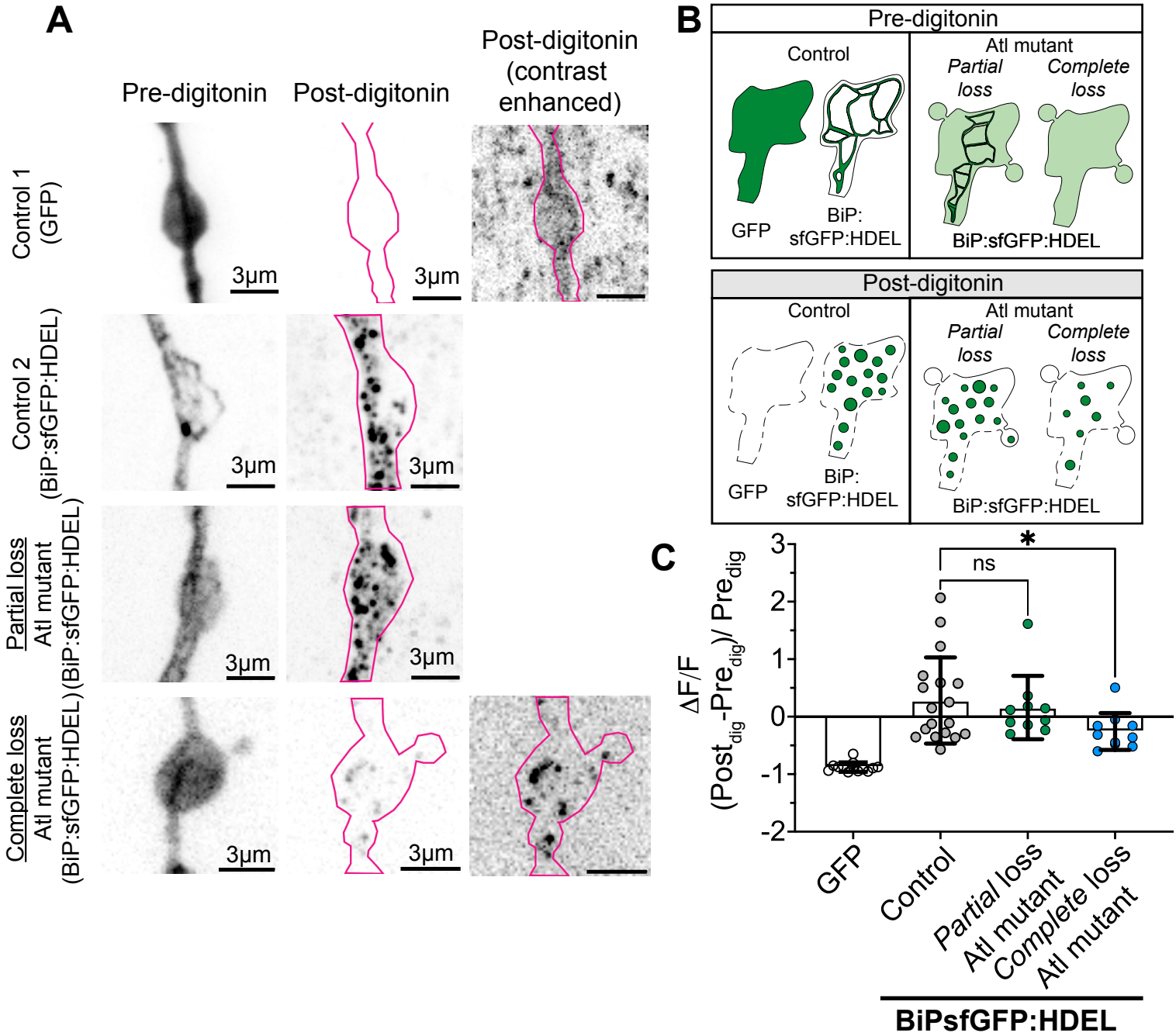

Figure 10-Figure Supplement 1

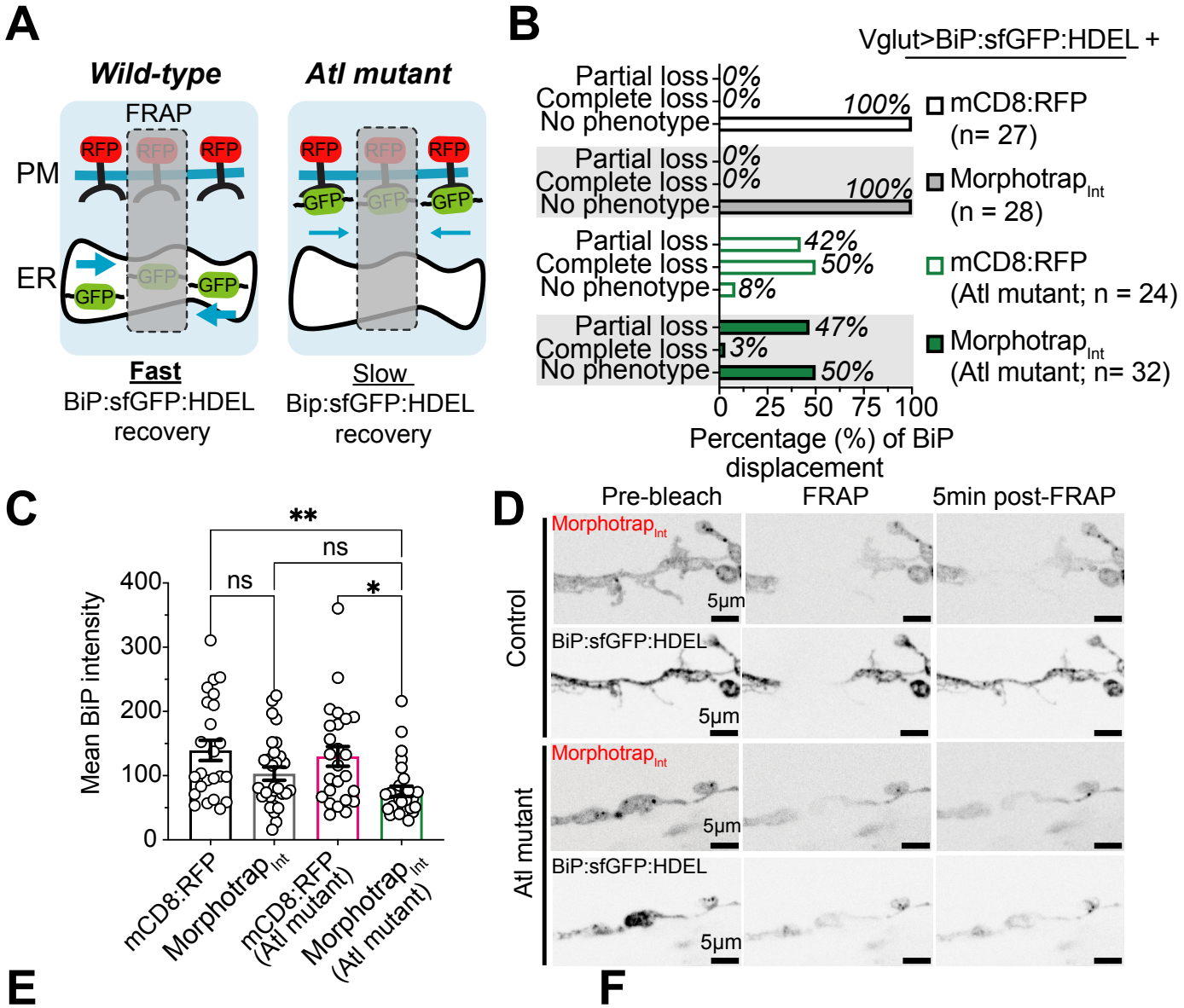

Best-fit values (one-phase association)		
Genotypes	Control	Atl mutant
Plateau (%)	19.60	17.11
Half Life (1/s)	83.39	83.39

p-value= 0.43

Best-fit values (one-phase association)		
Genotypes	Control	Atl mutant
Plateau (%)	57.07	38.35
Half Life (1/s)	53.23	45.76

p-value= <0.001

Figure 10